# Application of accretion torque models to
# the binary X-ray pulsars 4U 1626–67 and X Persei

(X 線連星パルサー 4U 1626–67 とペルセウス座 X への
降着トルクモデルの適用)

January, 2017

Physics Major
Graduate School of Science and Technology
Nihon University

Takagi Toshihiro

# ABSTRACT

We analyzed X-ray data of two binary X-ray pulsars, 4U 1626–67 and X Persei, observed by the GSC (Gas Slit Camera) contained in Monitor of All-sky X-ray Image (MAXI) mounted on the International Space Station. By using the epoch folding method, we derived the pulse period and pulse period derivative of 4U 1626–67 for every 60-d interval from 2009 October to 2013 September, and those of X Persei for every 250-d interval from 2009 October to 2016 Jun. In 4U 1626–67, the obtained results indicated that 4U 1626–67 was in spin-up phase for all the intervals, and the period derivative was correlated with the observed X-ray intensity, which corresponds to the 2–20 keV flux. The periods were agreed with those derived by the Fermi/GBM pulsar project. We then applied the accretion torque model in binary X-ray pulsars proposed by Ghosh & Lamb (1979) to the GSC data and past observations, which include both spin-up and spin-down phases, and confirmed that the model successfully explained the spin-up and spin-down behavior by changes of the X-ray intensity. Because the accretion torque model contains the mass and radius of the neutron star, the relation between the period derivative and X-ray intensity can constrain those values. If we assumed the nominal mass and radius of the neutron star, the source distance of 4U 1626–67 is obtained as 6–14 kpc, which is equivalent with that given by Chakrabarty (1998). Applying the above method to the observed relation of 4U 1626–67, we found that the mass and radius of the neutron star were obtained as $M = 1.34M_\odot$ and $R = 11.6$ km, although the result suffer from considerable systematic uncertainties. In X Persei, the derived period indicated that X Persei was in the spin-up phase, and its derivative is also correlated with the X-ray intensity. We applied the same technique to the GSC data, as well as the past observations including the spin-up and spin-down phases, and estimated the surface magnetic field of the neutrons star. The obtained result gave that the neutron star in X Persei prefer a relatively strong magnetic field of $B = (4 - 20) \times 10^{13}$ G, which is stronger than that of the neutron star in general binary X-ray pulsars. The value is consistent with that by a past study (Sasano, 2015).

# Contents

# List of Figures

# List of Tables

# Chapter 1

# INTRODUCTION

After the theoretical prediction of neutron stars (NSs) by Baade & Zwicky (1934), the evidence for NSs was discovered by radio observations by Hewish et al. (1968). Since then, about $10^4$ NSs have been found in the Milky Way and nearby galaxies, mainly through radio and X-ray observations. According to current understanding of stellar evolution, NSs are produced by supernova explosions of high-mass stars which initially have 8–20 solar mass (the solar mass is $M_\odot = 2.0 \times 10^{30}$ kg). An NS has typical mass of $M \sim 1.4 M_\odot$ and a typical radius of $R \sim 12$ km (e.g., reviews by Bhattacharyya (2010) and Özel (2013)). Because the mass and radius of NSs indicate very high density, they are suitable to investigate nuclear physics. Another important physical parameter of NSs is the magnetic field, $B = 10^{8-15}$ G.

In order to investigate the structure of NSs, many equation of states (EoSs) describing the relation between the pressure and the density were proposed theoretically. However, the correct EoS has not yet been uniquely identified. Because $M$ and $R$ are essential parameters to constrain the EoSs, various attempts to measure them have been carried out. The values of $M$ and $R$ were mainly obtained by binary motions of binary X-ray pulsars (BXPs) and X-ray bursts from weakly-magnetized NSs in binaries, respectively. The obtained $M$ and $R$ are not yet accurate enough to identify the correct EoS.

The values of $B$ of isolated NSs (e.g., radio pulsars) have been estimated from evolution of their rotation periods, assuming that they lose their rotational energy into magnetic dipole radiation. The derived values distribute over $B = 10^{8-15}$ G. Among then, those with the ultra-strong magnetic field ($B = 10^{14-15}$ G) are called magnetars, and their X-ray emission is thought to be powered by their magnetic energies. The above technique cannot be applied to BXPs, since their spin evolution is affected by the accretion torque. Instead, the magnetic fields of BXPs can be

accurately measured by the cyclotron resonance scattering features (CRSFs) in their spectra (e.g., Makishima et al. (1999)), because the resonance energy is proportional to $B$. The CRSF of BXPs typically appears at energies of 10–70 keV, indicating $B = (1 - 7) \times 10^{12}$ G. However, this technique becomes difficult for $B > 10^{13}$ G, because the CRSF in this case would appear at $> 100$ keV, where observations become much less sensitive than in lower energies. Therefore, it is not yet clear whether some BXPs have ultra-strong magnetic fields which are comparable to those of magnetars.

A BXP is a close binary system consisting of a mass-donating star (companion star) and a strongly-magnetized NS. The NS emit X-rays powered by accreting matter from the companion star, and the X-ray intensity exhibit clean modulation (pulsation) synchronized with the NS rotation. X-ray observations over the past 4 decades have established that a BXP generally spins up or spins down, by exchanging its angular momentum with the accreting matter. We hence expect that the pulse-period $P$ and its derivative $\dot{P}$ of a BXP should be correlated with its luminosity $L$. The relations between $\dot{P}$ and $L$ have been very crudely explained by theoretical models, including Rappaport & Joss (1977), Ghosh & Lamb (1979) (GL79 hereafter), and Lovelace et al. (1995) (LRB95 hereafter). The main parameters of the equation between $\dot{P}$–$L$ proposed by GL79 are $M$, $R$ and $B$. When the equation is calibrated accurately enough, the observed $\dot{P}$–$L$ relations are expected to give us observational constraints on $M$ and $R$, as well as $B$.

Monitor of All-sky X-ray Image (MAXI; Matsuoka et al. (2009)) is an X-ray all-sky monitor on the International Space Station, and has been scanning the whole sky every 92 min since 2009 August. MAXI observes long-time variability of X-ray sources. The GSC (Gas Slit Camera; Mihara et al. (2011); Sugizaki et al. (2011)), the main instrument of MAXI, detects X-rays in the 2–20 keV band. Because NSs in BXPs mainly emit X-rays in the band, the GSC is suitable to observe BXPs. Therefore, the MAXI/GSC data are useful to study the long-term variation of the X-ray intensity, $P$, and then $\dot{P}$.

In the present thesis, we analyze the MAXI/GSC data of two BXPs, and determine their flux, $P$, and $\dot{P}$. We then apply the spin-up/down models to the MAXI/GSC data, as well as the previous ones. By searching for a model that can best reproduce the observed $\dot{P}$–$L$ relations, we try to constrain $M$ and $R$ in one BXP, and estimate $B$ in the other.

# Chapter 2

# REVIEW

## 2.1 Neutron Stars

### 2.1.1 An overview

After the discovery of neutrons in 1932 by J. Chadwick, Baade & Zwicky (1934) predicted a theoretical concept of neutron stars (NSs), and suggested that NSs might be produced by supernova explosions. However, there was no observational evidence to confirm the prediction for over 30 years. In 1967, a radio pulsar (PSR B1919+21) which emits regular pulsation with a period of 1.3 s was discovered by Hewish et al. (1968). The radio emission is powered by rapid rotation of the NS. NSs were confirmed by them, and have been mainly found by radio and X-ray observations. Rigorously speaking, signals from an NS had already been detected in X-rays by Giacconi et al. (1962) in their discovery of cosmic X-ray sources, but it took a decade until the source, Scorpions X–1, was recognized as a mass-accreting NS.

According to the current understanding, NSs are produced by supernova explosions of high-mass stars which have 8-20 solar masses at their birth (the solar mass is $M_\odot = 2.0 \times 10^{30}$ kg). Since the pressure of degenerate neutrons competes with gravity, NSs do not collapse to a point. Typical NSs are considered to have the mass of $M = 1.4 - 2.0 M_\odot$ and radius of $R = 8 - 15$ km (e.g., reviews by Bhattacharyya (2010) and Özel (2013)). Such a small radius with a large mass gives a very high density to NSs. As a result, NSs are suitable to the investigation of physical states of matter at the high density close to that of nuclei, or even higher.

To understand the structure of NSs, equation of states (EoSs), which give the relation between the pressure and density of neutron matter, have been widely stud-

ied, and many equations were proposed. However, nobody knows the correct EoS. Because accurate knowledge of $M$ and $R$ can constrain the EoSs, many observations to measure them have been preformed so far. While $M$ are mainly derived from binary motions of binary X-ray pulsars (BXPs), $R$ are normally obtained by X-ray bursts from weakly-magnetized NSs in X-ray binaries. The obtained values are not yet accurate enough the requirements to determine the unique EoS. Therefore, the method which can derive an accurate $M$ and $R$ should be developed.

Another important parameter to describe the NS physics is the surface magnetic field strength $B$. In the case of isolated NSs (e.g., radio pulsars), the vales of $B$ have been estimated from changes of their rotation periods, because higher-$B$ objects will spin down more quickly, by emitting more luminous magnetic dipole radiation. The values have a broad distribution as $B = 10^{8-15}$ G. Resent observations revealed that NSs with ultra-strong magnetic fields ($B = 10^{14-15}$ G) emit X-rays which are probably powered by their magnetic energies, and these NSs are called magnetars. On the other hand, $B$ of NSs in BXPs have been derived from the cyclotron resonance scattering features (CRSFs) in their X-ray spectra (e.g., Makishima et al. (1999)), because the resonance energy of CRSFs is almost directly proportional to $B$. Although the technique is effective to measure the magnetic fields of $B \sim 10^{12}$ G which are equivalent to the resonance energies of 10–70 keV, we cannot easily utilize this method for objects with $B > 10^{13}$ G because of poorer photon statistics at higher energies.

## 2.1.2   The structure

As sketched in figure 2.1, NSs are considered to consist of several radial layers (for example, an outer crust, inner crust, outer core, and inner core). Pandharipande et al. (1976) summarized explanations of the state of expected layers as follows. The surface has relatively lower density ($\rho \leq 10^6$ g cm$^{-3}$) than the inner part of NSs, and its temperature and magnetic fields affect EoSs. The outer crust is a solid region ($10^6$ g cm$^{-3} \leq \rho \leq 4.3 \times 10^{11}$ g cm$^{-3}$) composed of a Coulomb lattice of heavy nuclei in $\beta$-equilibrium, and a relativistic degenerate electron gas. The inner crust ($4.3 \times 10^{11}$ g cm$^{-3} \leq \rho \leq 2.4 \times 10^{14}$ g cm$^{-3}$) consists of a lattice of neutron-rich nuclei, superfluid neutron gas and an electron gas. The neutron liquid ($2.4 \times 10^{14}$ g cm$^{-3} \leq \rho \leq 10^{15}$ g cm$^{-3}$) consists mainly of superfluid neutrons, a smaller concentration of superfluid protons, and normal electrons. The core ($\rho > 10^{15}$ g cm$^{-3}$), in which pion condensation is considered to take place, has a neutron solid or quark matter or other particles, with a density close to or even higher than that of nuclei. The properties

of these layers depend on the EoS. For example, stiff EoSs lead the density of $\rho \leq 10^{15}$ g cm$^{-3}$ in the center of NSs with $M = 1.4M_\odot$.
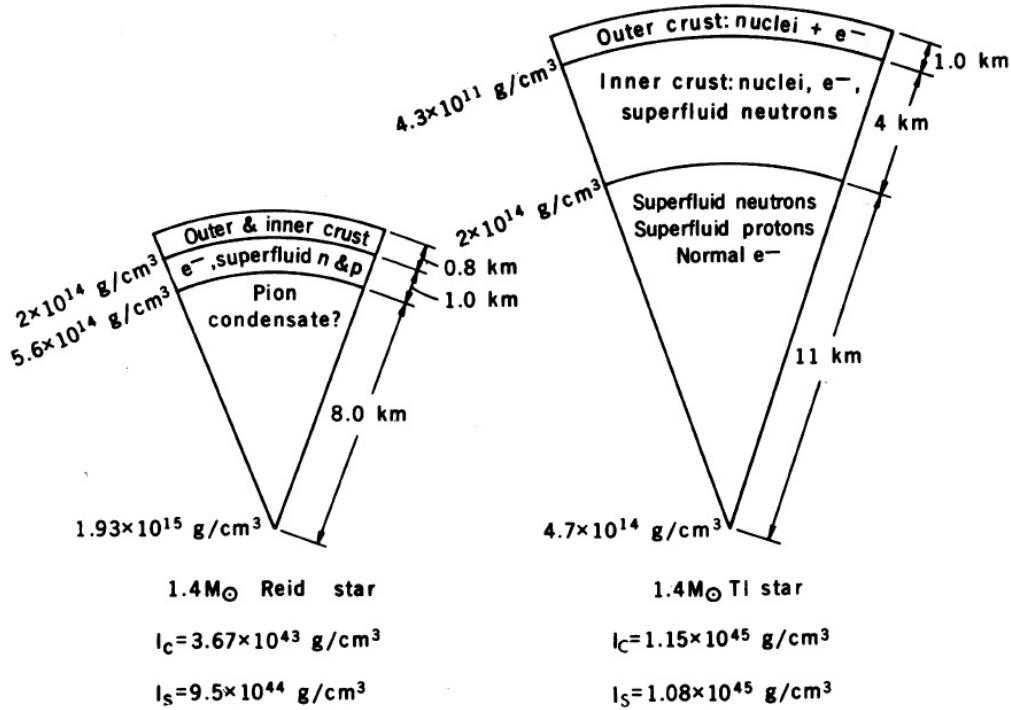


Figure 2.1: A sketch of the inner structure of NSs with $1.4M_\odot$ (Pines, 1980).

### 2.1.3 Equation of states

An EoS, describing the relation between the pressure and density of an NS, is the most fundamental theoretical concept that determines the NS structure. Once an EoS is specified, we can calculate the expected $M$ vs. $R$ relation. Conversely, simultaneous measurements of $M$ and $R$, on a sufficient number of NSs, is regarded as the best way to identify the correct EoS. Assuming that matter is composed of an ideal gas of free neutrons in a high density region, Oppenheimer & Volkoff (1939) proposed the first NS model. Since then, many EoSs have been developed. The EoSs can be classified into soft, moderate and stiff ones, according to the compressibility of the matter in an NS, which in turn depends on the nuclear force operating among neutrons (and protons). The proposed EoSs are accurate enough to theoretically calculate the crust of a model NS, although there are some unsolved theoretical problems. To identify the unique EoS, theoretical and observational studies are both important.

### 2.1.4   Mass and radius of neutron stars

In order to calculate a mass vs. radius relation of NSs, we need to specify an EoS, and combine it to an equation describing hydrostatic equilibrium between gravity and pressure, which the former has a variety depending on how to express the nuclear force, the latter is expressed uniquely by the general relativistic equation of hydrostatic equilibrium which is called the Tolman-Oppenheimer-Volkoff equation, given as

$$\frac{dP}{dr} = -\frac{\rho m}{r^2}\left(1 + \frac{P}{\rho}\right)\left(1 + \frac{4\pi P r^3}{m}\right)\left(1 - \frac{2m}{r}\right)^{-1}. \tag{2.1}$$

Here, $r$ is the radical coordinate, $P$ is the pressure, $\rho$ is its density, $m$ is the proton mass, the gravitational constant $G$ and the velocity of light $c$ is set unity. Combining this with the simplest EoS, namely, that of an ideal Fermi gas (ignoring particle-particle interactions though nuclear force), Oppenheimer & Volkoff (1939) then calculated the relation between the mass and density of an NS. They also gave the maximum mass $M_{VO}$ with the corresponding radius and the central density $\rho_{VO}$ as

$$M_{VO} = 0.7 M_\odot, \ R = 9.6 \text{ km}, \ \rho_{VO} = 5 \times 10^{15} \text{ g cm}^{-3}. \tag{2.2}$$

After the first calculation, more realistic theoretical models have been proposed by taking into account the nuclear force. By using the models together with the Tolman-Oppenheimer-Volkoff equation (equation 2.1), various results on the relations between $M$ and the central density, shown in figure 2.2 (left), were obtained. Figure 2.2 (right) shows the corresponding $M$ and $R$ curves. These results reveal a few general properties. A stiff EoS (e.g., BJ, TNI, TI and MF in figure 2.2 (left)) gives the maximum mass higher than that obtained from a soft EoS (e.g., R and $\pi$ in figure 2.2 (left)). An NS with a stiff EoS has a lower central density, a larger $R$ and a thicker crust, than that obtained from a soft EoS. If pion condensation occurs, the maximum mass of an NS decreases.

So far, EoSs have been developed, each giving the $M$ and $R$ curve of its own. Because the information on $M$ and $R$ can constrain EoSs, various observational attempts to measure $M$ and $R$ have been carried out. The obtained values are $M = 1.4 - 2.0 M_\odot$ (mainly from binary radio pulsars) and $R = 8 - 15$ km (mainly from weakly-magnetized neutron stars) (e.g. reviews by Bhattacharyya (2010) and Özel (2013)). Figure 2.3 compares the $M$ and $R$ curves derived from various EoSs with observed values of $M$. Thus, the observational information is not yet sufficient to constrain the unique EoS. Therefore, a new method which can derive an accurate $M$ and $R$ should be developed. We obviously need more information on $R$, and above
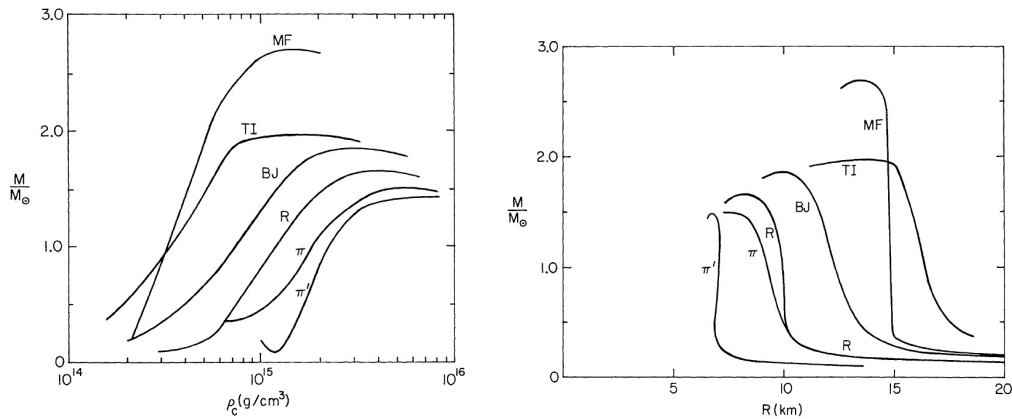
Figure 2.2: The NS mass $M$ calculated using various EoSs, shown as a function of the density (left) and of the radius (right). Both taken from (Baym & Pethick, 1979).

all, simultaneous $M$ and $R$ measurements from a fair number of objects.
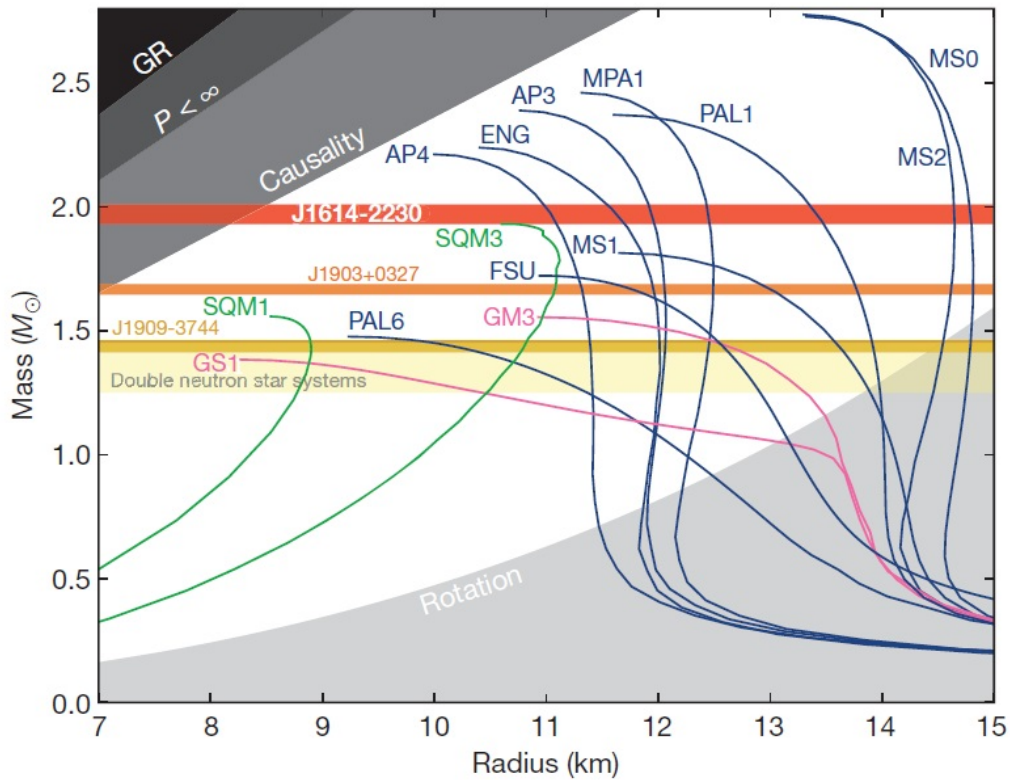


Figure 2.3: The $M$ and $R$ curves of NSs calculated from different EoSs (specified by different curves), and the observed values of $M$ for several representative NSs (Demorest et al., 2010).

### 2.1.5  Measurements of the mass

One of the key points in the observational study of NSs is measurements of their $M$. A good method to determine the mass of a star is to utilize the Kepler's third law. The method is also useful to obtain $M$ of an NS in binaries. The detail of that is as follows.

Let us consider a binary system with a circular orbit, consisting of two point-like stars which have the mass of $M_1$ and $M_2$. For simplicity, we may assume that $M_1$ refers to an NS, and $M_2$ to its optical companion. Let the separation of the binary system, and the distances between the stars and the barycenter be $a$, $a_1$ and $a_2$, respectively. Then, we have

$$a = a_1 + a_2, \tag{2.3}$$

$$M_1 a_1 - M_2 a_2 = 0. \tag{2.4}$$

Equations (2.3) and (2.4) give

$$a = \frac{M_1 + M_2}{M_2} a_1. \tag{2.5}$$

Because each star orbits around the barycenter, its pulsed emission suffers the effect of Doppler shift. The amplitude of this variation is directly proportional to the projected orbital velocity, which is expressed (for the component 1) as

$$v_1 = \frac{2\pi}{P_{orb}} a_1 \sin i, \tag{2.6}$$

where $P_{orb}$ is the orbital period, $i$ is the inclination angle which is the angle between the normal to the orbital plane and the line of sight. By measuring $P_{orb}$ and $v_1$, we can hence calculate $a_1 \sin i$. An independent constraint is available from the Kepler's third law, as

$$\frac{G(M_1 + M_2)}{a^3} = \left(\frac{2\pi}{P_{orb}}\right)^2. \tag{2.7}$$

From the above equations, we obtain

$$f_1 = \frac{(M_2 \sin i)^3}{(M_1 + M_2)^2} = \frac{P_{orb} \, v_1{}^3}{2\pi G}. \tag{2.8}$$

The function $f_1$ is called the mass function for the star with $M_1$, and depends only on the observed values, $P_{orb}$ and $v_1$ (or $a_1 \sin i$). Introducing the mass ratio $q$ between

the two components as

$$q = \frac{M_1}{M_2},$$ (2.9)

the equation to constrain $M_1$ can be written as

$$M_1 = \frac{f_1\, q\, (1 + q)^2}{\sin^3 i}.$$ (2.10)

If $q$ (or $M_2$) is somehow estimated, e.g., from optical spectroscopy of the companion, equation (2.9) and observed values ($P_{orb}$ and $v_1$) allow us to calculate $M_1$, although the equation still depends on $\sin i$.

To estimate $M$ of NSs, various methods including the above technique have been employed. The values of $M$ thus derived are shown in figure 2.4. While $M$ of an NS in a double NSs binary have very small errors, those of slow pulsars (BXPs) are not accurate enough.

## 2.1.6  Measurements of the radius

Another important quantity is $R$. The values of $R$ are obtained mainly from X-ray observations of thermonuclear X-ray bursts on the surface of an NS in low-mass X-ray binaries. Because the X-ray spectra of these bursts are usually described with a blackbody radiation model, the temperature $kT$ of the NS surface can be measured from observations. The luminosity $L$ of each burst is also calculated from the observed X-ray intensity $F$ and an assumed source distance $D$, as

$$L = 4\pi D^2 F.$$ (2.11)

Substituting the obtained $kT$ and $L$ into the Stefan-Boltzmann law,

$$L = 4\pi R^2 \sigma T^4,$$ (2.12)

we readily obtain $R$ as

$$R = D \left(\frac{F}{\sigma T^4}\right)^{\frac{1}{2}}.$$ (2.13)

The above measurements of $R$ are still inaccurate, hampered by, e.g., uncertainties in $D$ and possible deviation of the burst spectrum from a pure blackbody. As a result, the proposed EoSs in figure 2.3 cannot yet be constrained by the available observations. As can be seen there, accurate measurements of $R$, rather than $M$, are vitally needed.
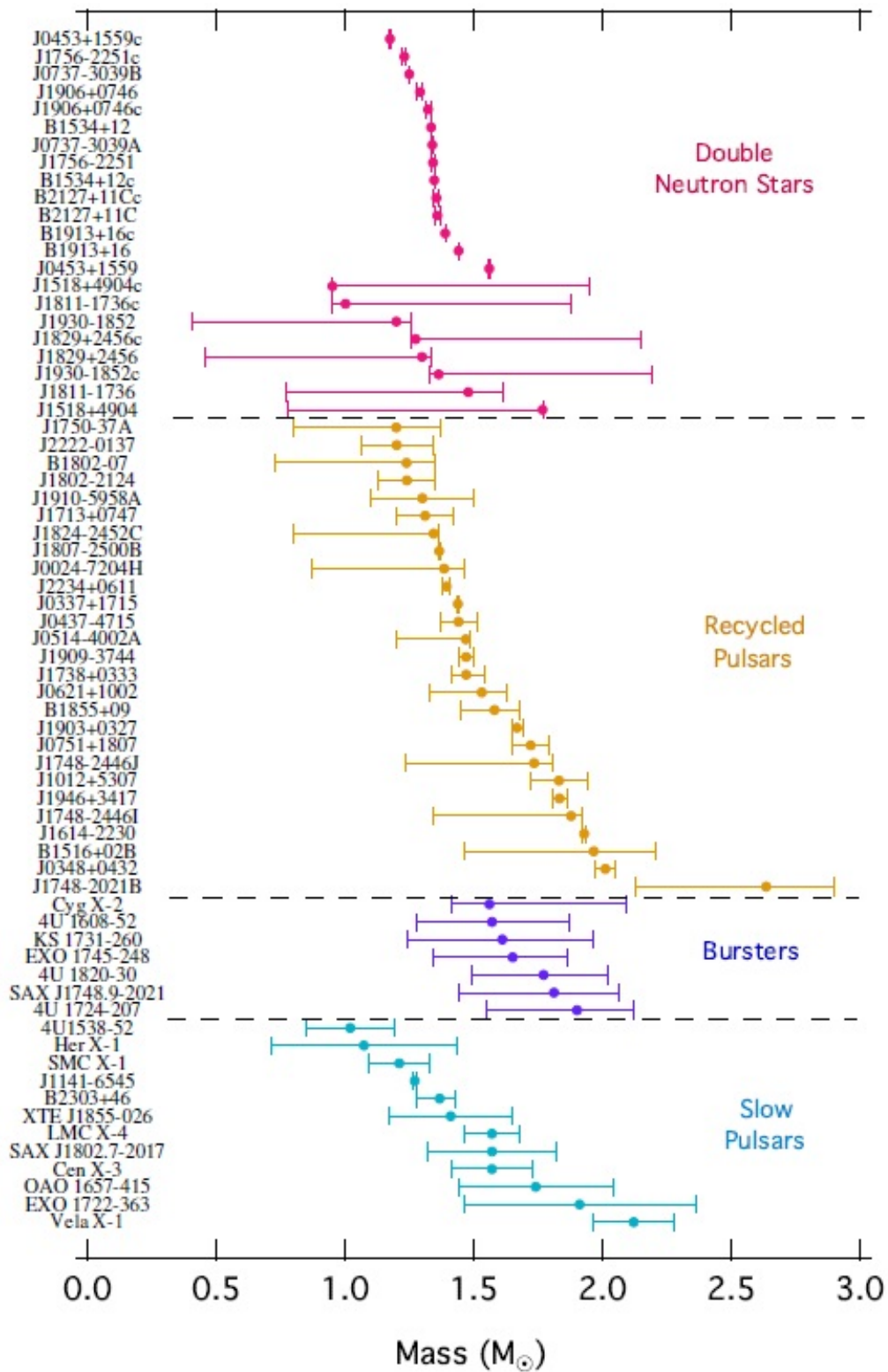
Figure 2.4: The values of *M* derived from various methods (Özel & Freire, 2016).

## 2.2 Binary X-ray Pulsars

### 2.2.1 An overview

In 1962, X-ray sources outside the solar system were discovered by Giacconi et al. (1962). So far, various classes of cosmic X-ray sources have been found. Among them, BXPs, which are a system consisting of a magnetized neutron star and a stellar companion, form one of the major classes. The coherent pulsations characterizing them were first detected from Cen X-3 by Giacconi et al. (1971) in 1971. Since then, some ~100 BXPs have been found in the Galaxy and the Magellanic Clouds. Because of strong interactions with accreting matter from a companion, their pulse periods $P$ are widely scattered, from ~50 ms to > $10^4$ s. The angular momentum of the accreting matter from a companion is considered to be transferred to the NS. The BXPs, then, show changes of $P$ (spin-up or spin-down) due to variabilities of the mass accretion rate $\dot{M}$. Figure 2.5 shows history of the variability of observed pulse frequencies. A mass transfer mode of BXPs is explained with Roche-Lobe overflow or stellar wind of a companion. When an accretion disk is formed around the NS in BXPs, the angular momentum of the accreting gas is transferred to the NS at the inner edge of the accretion disk, and accelerates the NS rotation until it finally reaches an equilibrium determined by $\dot{M}$ and $B$. If an NS rotation reaches the equilibrium, it shows spin-up and spin-down by small changes of X-ray intensity.
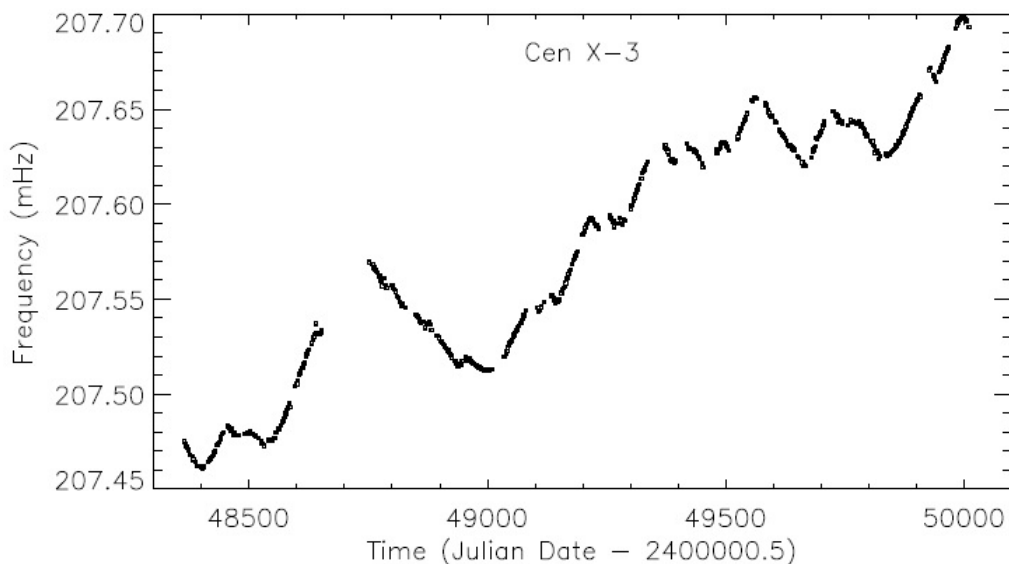


Figure 2.5: The history of pulse frequencies of Cen X-3 observed with BATSE (Bildsten et al., 1997).

The majority of BXPs are found in high-mass X-ray binaries which have high-mass ($> 10 M_\odot$) companion stars, while five BXPs have low-mass companions (LM-BXPs). About half of the BXPs with high-mass companions are Be X-ray binary pulsars (BeXBPs), which have Be star companions with optical emission lines (H$\alpha$ line) from a circumstellar disk. In this system, the accreting matter to the NS is supplied by the circumstellar disk, and an accretion disk is considered to be formed around the NS. The others are super giant X-ray binary pulsars (SGXBPs) consisting of OB super giant ($> 15 M_\odot$), and they are considered that the accreting matter to an NS is supplied by stellar wind of a companion. In LMBXPs, the accretion flow is considered to take place via Roche-Lobe overflow, and to form an accretion disk around the NS. Their properties are summarized in table 2.1.

Table 2.1: Properties of binary X-ray pulsars.

| Subclass | Companion | Mass Transfer Mode | Accretion Disk | Period (sec) |
|---|---|---|---|---|
| SGXBP | OB super giant ($\geq 15 M_\odot$) | Stellar wind capture | Usually absent[1] | $0.7$–$10^4$ |
| BeXBP | Be star ($10$–$20 M_\odot$) | Accretion from circumstellar disk | Yes | $2.8$–$5600$ |
| LMBXP | Low-mass star ($\leq 2 M_\odot$) | Roche-Lobe overflow | Yes | $1.2$–$140$ |

[1] Some very luminous ones (Cen X–3, SMC X–1) are considered to have disks.

The X-ray emission from an NS in a BXP is powered by gravitational energy of accreting matter, and the X-ray bolometric luminosity is written as

$$L = \frac{GM\dot{M}}{R}. \tag{2.14}$$

The X-ray spectrum is empirically described with an negative-positive exponential cutoff power-law (NPEX) model consisting of two power-law components and a common cutoff factor proposed by Mihara (1995). Some BXPs show CRSFs in their X-ray spectra, and the value of $B$ can be determined from its energy $E_a$ as

$$E_a = 11.6\, B_{12}\, (1 + z_g)^{-1}, \tag{2.15}$$

where $B_{12}$ is $B$ in units of $10^{12}$ G and $z_g$ is the gravitational redshift,

$$z_g = \left(1 - \frac{2GM}{Rc^2}\right)^{-\frac{1}{2}} - 1. \tag{2.16}$$

## 2.2.2 Accretion torque models

BXPs show the changes of $P$ due to variability of X-ray intensity, which reflects those of $\dot{M}$. We hence expect that $\dot{P}$ is correlate with $\dot{M}$. The correlation can be basically explained as follows.

The matter at a distance $R_K$ from the center of the NS, rotates with the Keplerian velocity $V_K$, as

$$V_K = (GMR_K)^{\frac{1}{2}}. \tag{2.17}$$

The radius $R_A$ at which the magnetic pressure is equal to the gas pressure is called the Alfven radius, and is though to scale as

$$R_A \propto \mu^{\frac{4}{7}} L^{-\frac{2}{7}}, \tag{2.18}$$

where $\mu$ is the magnetic dipole moment of the NS. At $R_A$, the matter transfers its angular momentum to the NS and accretes onto the NS along magnetic field lines. The rate of this angular momentum is written as

$$N_{AC} = \dot{M}V_K R_A. \tag{2.19}$$

This $N_{AC}$ is expected to cause the angular momentum of the NS $N_{NS}$ to change as

$$N_{AC} = I\dot{\omega}, \tag{2.20}$$

where $I$ is the moment of inertia of the NS and $\dot{\omega}$ is derivative of the angular velocity $\omega$ of the NS. Obviously, we have

$$\dot{\omega} = 2\pi\dot{\nu} = 2\pi\left(-\frac{\dot{P}}{P^2}\right), \tag{2.21}$$

where $\dot{\nu}$ is the frequency derivative and $\dot{P}$ is the pulse-period derivative. From equations (2.18), (2.19) and (2.20), the relation between $\dot{\omega}$ and $L \propto \dot{M}$ is given as

$$\dot{\omega} \propto \mu^{\frac{2}{7}} I^{-1} L^{\frac{6}{7}}. \tag{2.22}$$

Finally, the equation between $\dot{P}$ and $L$ is obtained as

$$-\frac{\dot{P}}{P^2} \propto \mu^{\frac{2}{7}} \, I^{-1} \, L^{\frac{6}{7}}. \tag{2.23}$$

The above simple view of interactions between the NS magnetosphere and accretion flow have been developed into several more detailed models. Rappaport & Joss (1977), Ghosh & Lamb (1979), Lovelace et al. (1995), and Bozzo et al. (2009) proposed their accretion models and presented respective equations describing $\dot{P}$ as a function of $L$, $P$, $M$, $R$ and $B$ of the NS. These models have been compared with observational data by Joss & Rappaport (1984), Finger et al. (1996), Reynolds et al. (1996), Bildsten et al. (1997), Klochkov et al. (2009) and Sugizaki et al. (2015). The results show that the observed $\dot{P}$–$L$ relations are mostly consistent with the model predictions. However, the validity of the models has not yet been fully confirmed, because a detailed comparison would requires long-term monitoring of some suitable objects with known $B$, covering significant $P$ and $L$ ranges with a sufficient sampling rate. When these models describing the accretion torque are better calibrated, the observed $\dot{P}$–$L$ relations can give us observational constraints on $M$ and $R$. Therefore, further studies of the $\dot{P}$–$L$ relations are expected to be valuable.

### 2.2.3   The Ghosh & Lamb model

To determine the coefficient of proportionality in equation 2.23, Ghosh & Lamb (1979) (hereafter GL79) assumed that the accreting matter transfers the angular momentum to the NS at the "outer transition zone", $r_0$. According to equation (11) in GL79, it is given as $r_0 = 0.52 \, r_{\mathrm{A}}^{(0)}$, where $r_{\mathrm{A}}^{(0)}$ is the characteristic Alfven radius. Substituting the numbers, we obtain

$$r_{\mathrm{A}}^{(0)} = 3.2 \times 10^8 \, \dot{M}_{17}^{-\frac{2}{7}} \, \mu_{30}^{\frac{4}{7}} \left(\frac{M}{M_\odot}\right)^{-\frac{1}{7}} \mathrm{cm}, \tag{2.24}$$

$$r_0 = 1.7 \times 10^8 \, \dot{M}_{17}^{-\frac{2}{7}} \, \mu_{30}^{\frac{4}{7}} \left(\frac{M}{M_\odot}\right)^{-\frac{1}{7}} \mathrm{cm}, \tag{2.25}$$

where $\dot{M}_{17}$ is $\dot{M}$ in units of $10^{17}$ g s$^{-1}$ and $\mu_{30}$ is $\mu$ in units of $10^{30}$ G cm$^3$.

In this way, GL79 gave their theoretical $\dot{P}$–$L$ relation [equation (15) in GL79] as

$$\dot{P} = -5.0 \times 10^{-5} \, \mu_{30}^{\frac{2}{7}} \, n(\omega_{\mathrm{s}}) \, S_1(M) \, P^2 \, L_{37}^{\frac{6}{7}} \, \mathrm{s \, yr}^{-1}, \tag{2.26}$$

or

$$\dot{\nu} = -\frac{\dot{P}}{P^2} = 5.8 \times 10^{-10} \, \mu_{30}^{\frac{2}{7}} \, n(\omega_s) \, S_1(M) \, L_{37}^{\frac{6}{7}} \text{ Hz s}^{-1}, \qquad (2.27)$$

where $L_{37}$ is $L$ in units of $10^{37}$ erg s$^{-1}$ and $L$ is defined by $L = \dot{M}(GM/R)$. The functions $n(\omega_s)$ and $S_1(M)$ are described respectively by equations (10) and (17) in GL79 as

$$n(\omega_s) \approx 1.39 \, [1 - \omega_s \, \{4.03 \, (1 - \omega_s)^{0.173} - 0.878\} \,] \, (1 - \omega_s)^{-1}, \qquad (2.28)$$

$$S_1(M) = R_6^{\frac{6}{7}} \left(\frac{M}{M_\odot}\right)^{-\frac{3}{7}} I_{45}^{-1}, \qquad (2.29)$$

where $R_6$ is $R$ in units of $10^6$ cm and $I_{45}$ is $I$ in units of $10^{45}$ g cm$^2$. Here, $\omega_s$ is the so-called fastness parameter, which is a dimensionless parameter, defined as the ratio of the pulsar's angular frequency to the Keplerian angular frequency of the accreting matter at $r_0$. This $\omega_s$ is expressed approximately by equation (16) in GL79 as

$$\omega_s \approx 1.35 \, \mu_{30}^{\frac{6}{7}} \, S_2(M) \, P^{-1} \, L_{37}^{-\frac{3}{7}}. \qquad (2.30)$$

Here, $S_2(M)$ is given by equation (18) in GL79 as

$$S_2(M) = R_6^{-\frac{3}{7}} \left(\frac{M}{M_\odot}\right)^{-\frac{2}{7}}. \qquad (2.31)$$

Equation (2.28) is effective in $\omega_s = 0 - 0.9$ and is accurate within 5%. The behavior of $n(\omega_s)$ is plotted in figure 2.6. The zero crossover point is located at $\omega_s \sim 0.349$, below which the equation is positive and above which it is negative.

## 2.2.4   The Lovelace model

To explain the relation between $\dot{P}$ and $\dot{M}$, Lovelace et al. (1995) (hereafter LRB95) took into account not only the torque from the accreting matter, but also magnetic outflows and magnetic breaking. After many numerical integrations they introduced a characteristic radius $r_{\text{to}}$, where the angular velocity $\omega_a$ of accreting matter reaches the maximum ($\text{d}\omega_a/\text{d}r = 0$), and hence the matter transfers the angular momentum to the NS therein. This $r_{\text{to}}$ is given by equation (16) in LRB95 as

$$r_{\text{to}} \approx 0.91 \times 10^8 \left(\frac{\alpha D_{\text{m}}}{0.1}\right)^{0.3} \mu_{30}^{0.57} \, \dot{M}_{17}^{-0.3} \left(\frac{M}{M_\odot}\right)^{-0.15} \text{cm}, \qquad (2.32)$$
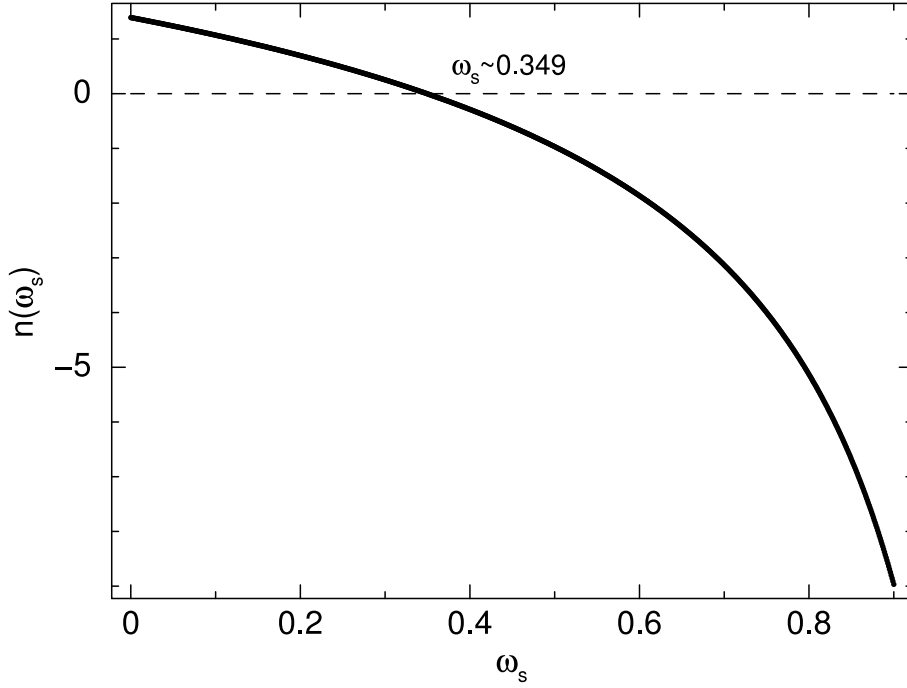
Figure 2.6: The approximation function $n(\omega_s)$ defined in equation 2.28, plotted against $\omega_s$ (Takagi et al., 2016).

where $\alpha$ is the viscous parameter in Shakura & Sunyaev (1973) and $D_m$ is the magnetic diffusivity parameter. In LRB95, $\alpha$ is assumed as 0.01 to 0.1 and $D_m$ is of order unity. Basically, $r_{to}$ has the same nature as $r_0$ in the GL79 model [equation (2.25)].

Further employing the corotation radius defined as

$$r_{cr} \equiv \left(\frac{GM}{\omega_*{}^2}\right)^{\frac{1}{3}} \approx 1.5 \times 10^8 \left(\frac{M}{M_\odot}\right)^{\frac{1}{3}} P^{\frac{2}{3}} \text{ cm}, \tag{2.33}$$

where $\omega_* = 2\pi/P$ is the NS's rotation angular frequency, LRB95 classify the behavior into a magnetic outflow case ($r_{to} < r_{cr}$), and a case of magnetic braking of the disk ($r_{to} > r_{cr}$). When $r_{to}$ is smaller than $r_{cr}$, the NS shows spin-up with magnetic outflow. Equation (18b) in LRB95 describes $\dot{P}$ in terms of $\dot{M}$ and $r_{to}$, and the equation can be rewritten as

$$\dot{P} \approx -5.8 \times 10^{-5} P^2 \dot{M}_{17} I_{45}^{-1} \left(\frac{M}{M_\odot}\right)^{\frac{1}{2}} \left(\frac{r_{to}}{10^8 \text{ cm}}\right)^{\frac{1}{2}} \text{ s yr}^{-1}. \tag{2.34}$$

By substituting $\dot{M} = LR/GM$, we obtain

$$\dot{P} \approx -4.3 \times 10^{-5}\, \mu_{30}{}^{0.285} \left(\frac{\alpha D_\mathrm{m}}{0.1}\right)^{0.15} R_6{}^{0.85} \left(\frac{M}{M_\odot}\right)^{-0.425} I_{45}{}^{-1}\, P^2\, L_{37}{}^{0.85}\ \mathrm{s\ yr^{-1}},\quad (2.35)$$

which is equivalent to equation (2.26) of GL79. The indices are the same, and the factor is almost the same. The difference is the $\alpha D_\mathrm{m}$ factor instead of the $n(\omega_\mathrm{s})$ factor.

When $r_\mathrm{to}$ is larger than $r_\mathrm{cr}$, magnetic braking takes place. It can work for either spin-up or spin-down, although it mostly works as spin-down.

## 2.3 4U 1626–67

4U 1626–67 is a low-mass X-ray binary pulsar first detected with the Uhuru satellite (Giacconi et al., 1972), and its 7.6-s coherent pulsation was discovered by Rappaport et al. (1977). Because no period modulation due to orbital motion has been detected beyond an upper limit of $a_\mathrm{x} \sin i \leq 13$ lt-ms ($a_\mathrm{x}$ is the orbital semi-major axis of the NS and $i$ is the orbital inclination angle), the mass of the companion star is estimated to be very low ($\sim 0.03 - 0.09 M_\odot$ for $11° \leq i \leq 36°$; Levine et al. (1988)). It is hence classified as an ultra compact X-ray binary (van Haaften et al., 2012). The BeppoSAX observation revealed a CRSF at $\sim 37$ keV, indicating $B = 3.2 \times 10^{12}\,(1 + z_\mathrm{g})$ G (Orlandini et al., 1998). The feature was confirmed by the Suzaku observation (Iwakiri et al., 2012). The source distance was estimated to be 5–13 kpc from the optical flux by assuming that the effective X-ray albedo of the accretion disk is high ($\gtrsim 0.9$) (Chakrabarty, 1998).

Since the discovery of the 7.6-s pulsation in 1977, the values of $P$ of 4U 1626–67 has been repeatedly measured with various X-ray satellites (e.g. references in Chakrabarty et al. (1997); Camero-Arranz et al. (2010)). Table 2.2 and 2.3 summarize the X-ray fluxes, $P$, and $\dot{P}$ observed from 1978 to 2008, and figure 2.7 visualizes long-term behavior of these quantities. It clearly shows that the source made transitions twice between the spin-up and the spin-down phases, at MJD $\sim$ 48000 (1990 June) and MJD $\sim$ 54000 (2008 February), separated by $\sim 18$ years. In each phase, $\dot{P}$ was almost constant, and its absolute values were very similar as $|\dot{P}| = 2 \sim 5 \times 10^{-11}$ s s$^{-1}$. This period-change behavior suggests that 4U 1626–67 is close to an equilibrium state in which the net torque transfer from the accreting matter to the NS is approximately zero. At the last transition in 2008, when the source turned from the spin-down into the spin-up phase, the X-ray flux increased

by a factor of ~2.5 (Camero-Arranz et al., 2010).  These properties, together with
the accurate knowledge of $B$, make this object ideal for our study.
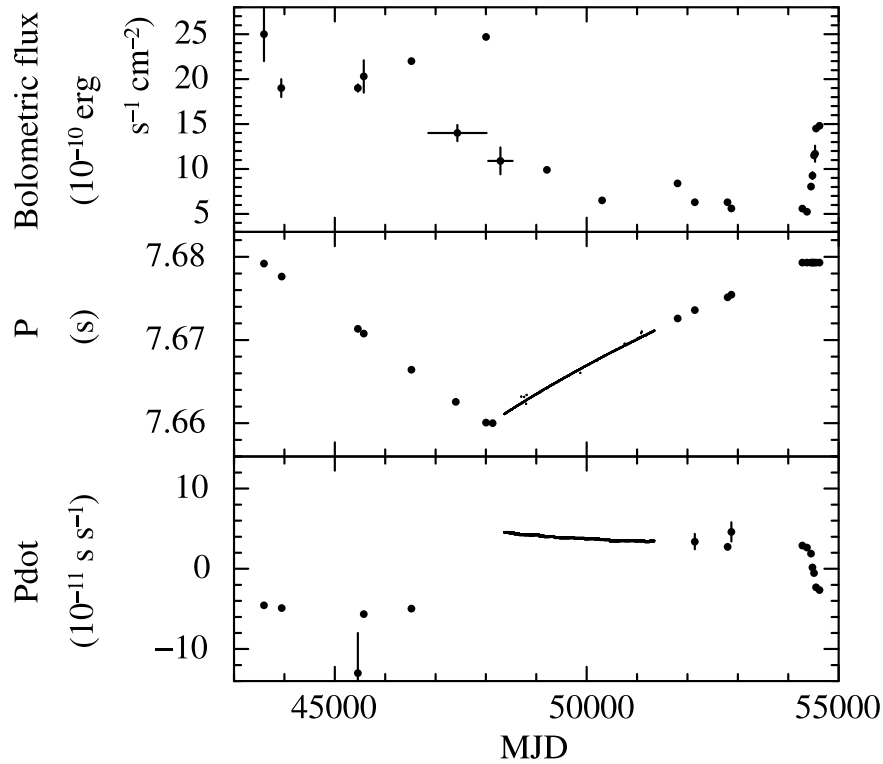


Figure 2.7: Bolometric flux (top), $P$ (middle) and $\dot{P}$ (bottom) of 4U 1626–67 obtained by past X-ray observations from 1978 to 2008 (Takagi et al., 2016).  In the top panel, observed X-ray intensities are converted to the model flux in the 0.5–100 keV band assuming the typical spectral model given by Camero-Arranz et al. (2012). Filled circles and solid lines represent the past observations in table 2.2 and 2.3, and BATSE observations[2], respectively.

---

[2]http://gammaray.nsstc.nasa.gov/batse/pulsar/data/sources/4u1626.html

Table 2.2: X-ray flux, period and period derivative obtained in past observations of 4U 1626–67 (1).

| Observation Date | Flux | | | | Pulsation | | | Ref.[3] |
| --- | --- | --- | --- | --- | --- | --- | --- | --- |
| | Period (MJD) | Band (keV) | Obs. $(10^{-10}$ erg s$^{-1}$ cm$^{-2})$ | Bolometric[1] | Epoch (MJD) | $P^2$ (s) | $\dot{P}$ $(10^{-11}$ s s$^{-1})$ | |
| 1978 Mar | 43596 | 0.7–60 | 24 ± 3 | 25 ± 3 | 43596.7 | 7.679190(26) | −4.55[4] | (1) |
| 1979 Feb | 43928–43946 | 2–10 | 5.1 ± 0.3 | 19 ± 1 | 43946.0 | 7.677632(13) | −4.9 ± 0.1[4] | (2) |
| 1983 May | 45457–45459 | 2–20 | 10.1 ± 0.2 | 19.0 ± 0.4 | 45458.0 | 7.671350(1) | −13 ± 5 | (3) |
| 1983 Aug | 45576 | 2–10 | 5.6 ± 0.5 | 20.3 ± 1.8 | 45576.9 | 7.67077(1) | −5.65 ± 0.10[5] | (4) |
| 1986 Mar | 46519–46520 | 1–20 | 14 ± 0.4[6] | 22 ± 0.7 | 46520.0 | 7.6664220(5) | −4.96 ± 0.06[4] | (5) |
| 1987 Mar | 46855–48012 | 1–20 | 8.89 ± 0.56 | 14.0 ± 0.9 | | | | (6) |
| 1988 Aug | | | | | 47400.3 | 7.6625685(30) | | (7) |
| 1990 Apr | 47999–48002 | 2–60 | ~ 20.6 | ~ 24.7 | 48001.1 | 7.660069(2) | | (8) |
| 1990 Jun | 48043–48530 | 1–20 | 6.67 ± 0.89 | 10.9 ± 1.5 | | | | (6) |
| 1990 Aug | | | | | 48133.5 | 7.66001(4) | | (4) |
| 1993 Aug | 49210–49211 | 0.5–10 | ~ 2.8 | ~ 9.9 | | | | (9) |
| 1996 Aug | 50301–50306 | 2–60 | ~ 6.1 | ~ 6.5 | | | | (10) |

All errors represent 1-σ uncertainties.

[1] Converted 0.5–100 keV flux, assuming the spectral models in Camero-Arranz et al. (2012).

[2] Values in parentheses are 1 σ error in the last digit(s).

[3] (1) Pravdo et al. (1979) (HEAO 1/A-2), (2) Elsner et al. (1983) (Einstein/MPC), (3) Kii et al. (1986) (Tenma), (4) Mavromatakis (1994) (EXOSAT/GSPC, ROSAT), (5) Levine et al. (1988) (EXOSAT/ME), (6) Vaughan & Kitamoto (1997) (Ginga/ASM), (7) Shinoda et al. (1990) (Ginga), (8) Mihara (1995) (Ginga), (9) Angelini et al. (1995) (ASCA), (10) Orlandini et al. (1998) (BeppoSAX), (11) Krauss et al. (2007) (Chandra, XMM-Newton), (12) The data were read from figure 4 in Camero-Arranz et al. (2010) (Swift/BAT), (13) Camero-Arranz et al. (2010) (RXTE/PCA spectra).

[4] Averaged value.

[5] Averaged $\dot{P}$ calculated from $P$ of the observation and the previous one in this table.

[6] The error was estimated by the count rate with ME, using the values of the count rate and the error with GSPC.

[7] Absorption-corrected flux.

Table 2.3: X-ray flux, period and period derivative obtained in past observations of 4U 1626–67 (2).

| Observation Date | Period (MJD) | Band (keV) | Obs. $(10^{-10}$ erg s$^{-1}$ cm$^{-2}$) | Bolometric[1] | Epoch (MJD) | $P$[2] (s) | $\dot{P}$ $(10^{-11}$ s s$^{-1})$ | Ref.[3] |
|---|---|---|---|---|---|---|---|---|
| | | | Flux | | | Pulsation | | |
| 2000 Sep | 51803 | 0.3–10 | 2.4[7] | 8.4 | 51803.6 | 7.6726(2) | | (11) |
| 2001 Aug | 52145 | 0.3–10 | 1.8[7] | 6.3 | 52145.1 | 7.6736(2) | $3.39 \pm 0.96$[5] | (11) |
| 2003 Jun | 52793 | 0.3–10 | 1.8[7] | 6.3 | 52795.1 | 7.67514(5) | $2.74 \pm 0.37$[5] | (11) |
| 2003 Aug | 52871 | 0.3–10 | 1.6[7] | 5.6 | 52871.2 | 7.67544(6) | $4.6 \pm 1.2$[5] | (11) |
| 2007 Jun | 54280 | 15–50 | $2.8 \pm 0.1$ | $5.6 \pm 0.2$ | 54280 | ~7.6793 | 2.9 | (12) |
| 2007 Sep | 54370 | 15–50 | $2.6 \pm 0.1$ | $5.2 \pm 0.2$ | 54370 | ~7.6793 | 2.7 | (12) |
| 2007 Dec | 54450 | 15–50 | $4.0 \pm 0.1$ | $8.0 \pm 0.3$ | 54450 | ~7.6793 | 1.9 | (12) |
| 2008 Jan | 54480 | 15–50 | $4.6 \pm 0.2$ | $9.3 \pm 0.4$ | 54480 | ~7.6793 | 0.18 | (12) |
| 2008 Feb | 54510 | 15–50 | $4.6 \pm 0.1$ | $11.5 \pm 0.3$ | 54510 | ~7.6793 | −0.53 | (12) |
| 2008 Mar | 54530 | 2–100 | $10.1 \pm 0.8$ | $11.7 \pm 0.9$ | | | | (13) |
| 2008 Mar | 54550 | 15–50 | $5.8 \pm 0.1$ | $14.5 \pm 0.3$ | 54550 | ~7.6793 | −2.3 | (12) |
| 2008 Jun | 54620 | 15–50 | $5.9 \pm 0.1$ | $14.8 \pm 0.2$ | 54620 | ~7.6793 | −2.7 | (12) |

All errors represent 1-$\sigma$ uncertainties.

[1] Converted 0.5–100 keV flux, assuming the spectral models in Camero-Arranz et al. (2012).

[2] Values in parentheses are 1 $\sigma$ error in the last digit(s).

[3] (1) Pravdo et al. (1979) (HEAO 1/A-2), (2) Elsner et al. (1983) (Einstein/MPC), (3) Kii et al. (1986) (Tenma), (4) Mavromatakis (1994) (EXOSAT/GSPC, ROSAT), (5) Levine et al. (1988) (EXOSAT/ME), (6) Vaughan & Kitamoto (1997) (Ginga/ASM), (7) Shinoda et al. (1990) (Ginga), (8) Mihara (1995) (Ginga), (9) Angelini et al. (1995) (ASCA), (10) Orlandini et al. (1998) (BeppoSAX), (11) Krauss et al. (2007) (Chandra, XMM-Newton), (12) Camero-Arranz et al. (2010) (RXTE/PCA spectra).

Camero-Arranz et al. (2010) (Swift/BAT), (13) Camero-Arranz et al. (2010) (RXTE/PCA spectra).

[4] Averaged value.

[5] Averaged $\dot{P}$ calculated from $P$ of the observation and the previous one in this table.

[6] The error was estimated by the count rate with ME, using the values of the count rate and the error with GSPC.

[7] Absorption-corrected flux.

## 2.4 X Persei

4U 0352+309 (hereafter X Persei) is a Be X-ray binary pulsar consisting of an NS with a long pulse period of $\sim$ 835 s (White et al., 1976) and a Be star (X Persei). Although it has a relatively low luminosity ($L \sim 10^{35}$ erg s$^{-1}$), its nearby distance, 0.7–1.3 kpc (Lutovinov et al., 2012), makes it a relatively bright X-ray source. X Persei has the orbital period of $\sim$ 250 d and a small eccentricity ($e \sim 0.11$) (Delgado-Martí et al., 2001). Then, the binary orbit is wide, and is approximately circular unlike many other BeXBPs.

Since the source is persistent bright, many X-ray satellites have observed it and derived its $P$ for a long time (e.g., Acuner et al. (2014)). It then became clear that the source shows both spin-up and spin-down behavior. As shown in the pulse-period history in figure 2.8, the source was in a spin-up phase with $\dot{P}/P \sim -1.5 \times 10^4$ yr$^{-1}$ before 1978, and showed spin-down with $\dot{P}/P \sim -1.3 \times 10^4$ yr$^{-1}$ from 1978 to 2002. At present, X Persei is a in spin-up phase with $\dot{P}/P \sim -3.6 \times 10^4$ yr$^{-1}$ (Acuner et al., 2014).
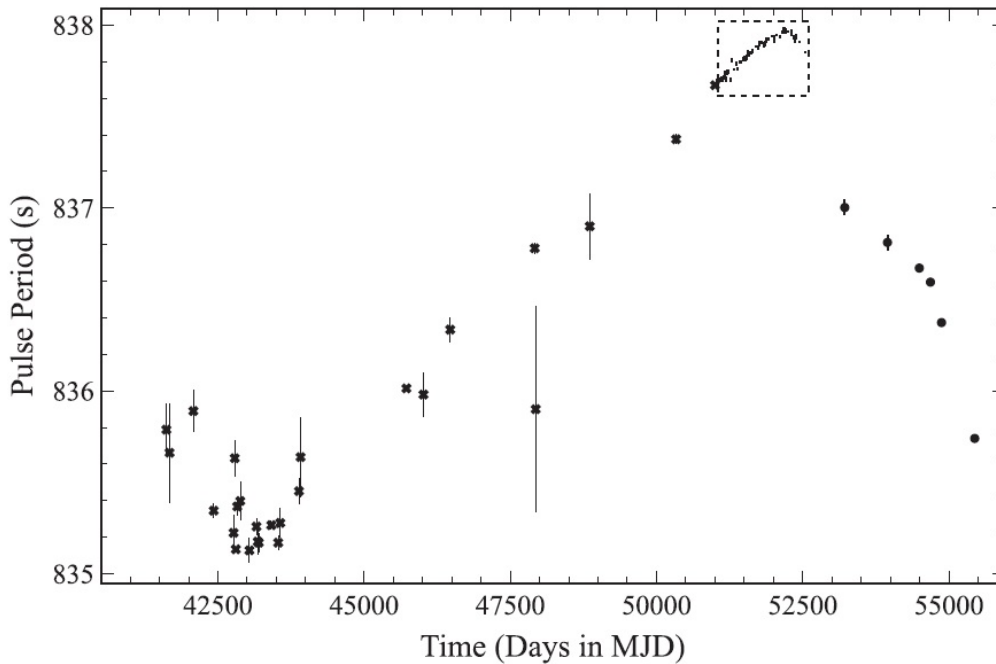


Figure 2.8: The history of the observed $P$ of X Persei (Acuner et al., 2014).

Using satellites such as BeppoSAX (Di Salvo et al., 1998) and Suzaku (Sasano, 2015), the X-ray spectra of X Persei have been measured over broad energy bands, typically from < 1 keV up to 100–200 keV. In energies below $\sim$ 20 keV, the spec-

trum of X Persei is approximated by a power-law with the photon index $\Gamma \sim 2.2$, which is somewhat steeper than those of other BXPs (typically $\Gamma = 1.0 - 1.5$). In the 20–100 keV band where those of other BXPs all exhibit steep cutoff properties, the spectra of X Persei is significantly harder, and continues to $> 100$ keV with a very mild cutoff. These features are considered to suggest that X Persei has rather strong magnetic field of $> B^{13}$ G (Sasano, 2015). On the other hand, in the 4–200 keV spectrum taken with INTEGRAL, Lutovinov et al. (2012) reported an absorption feature at $\sim 23.5$ keV, and attributed it to a CRSF corresponding to $B = (2.4 - 2.9) \times 10^{12}$ G. However, the feature is very shallow and broad, and is likely to be an artifact caused by wrong continuum modeling (Doroshenko et al. (2012); Sasano (2015)).

# Chapter 3

# INSTRUMENT

## 3.1  Monitor of All-sky X-ray Image

Monitor of All-sky X-ray Image (MAXI; Matsuoka et al. (2009)) is an X-ray all-sky monitor mounted on the Japanese Experiment Module of the International Space Station (ISS). MAXI was launched by Space Shuttle Endeavor in 2009 July, and has operated for over 7 years by the members of MAXI team consisting of Japan Aerospace Exploration Agency (JAXA), Institute of Physical and Chemical Research (RIKEN) and X-ray astronomy groups in several Japanese universities. The main purposes of the MAXI mission are detections of new transients which include binary X-ray pulsars (BXPs), and to observe the changes of known X-ray sources (e.g., history of pulse periods and flux variations). Since the in-orbit operation started in 2009 August, MAXI has been scanning the whole sky every 92 min which is the orbital period of the ISS. Therefore, MAXI can observe not only new X-ray transients but also long-time variability of X-ray sources. The information of these events has been reported by the MAXI team to the astronomers over the world, and encourages follow-up observations with X-ray satellites, as well as multi wavelength observations. Figure 3.1 shows the all-sky map obtained by MAXI.

Figure 3.2 shows an overview of MAXI. MAXI has two different types of X-ray detectors which are the Gas Slit Camera (GSC; Mihara et al. (2011); Sugizaki et al. (2011)) consisting of one-dimensional gas proportional counters sensitive to X-rays in the 2–20 keV band and the Solid-state Slit Camera (SSC; Tomida et al. (2011)) composed of X-ray charge-coupled-devices (CCDs) covering the X-ray energy of 0.7–7.0 keV. Because the GSC has a good time resolution (0.1 ms) and a large effective area (5350 cm$^2$), and covers the main energy band (2–20 keV) in which

---

[1]`http://maxi.riken.jp/top/`
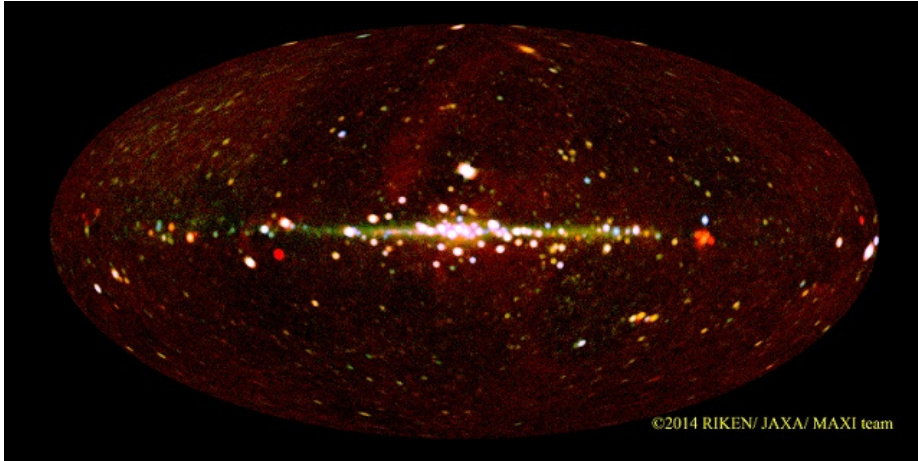
Figure 3.1: The 4.6-year all-sky map obtained from MAXI [1].

neutron stars of BXPs emit X-rays, it is suitable to study the sources. For these reasons, we used only GSC data in this study.

## 3.2  Gas Slit Camera

The GSC, the main instrument of MAXI, is composed of one-dimensional gas proportional counters and collimators (figure 3.3), and has field of views (FoVs) of the horizontal direction and the zenithal direction. The proportional counters are sensitive to X-ray photons of 2–20 keV, and have six parallel carbon wires with one-dimensional position sensitivity. Directions of X-ray photons are determined by collimators which limit the FoVs in the orthogonal direction to the wires. The GSC has a detection area of 5350 cm$^2$ in total and high sensitivity which is better than previous all-sky monitors in the 2–20 keV band (see table 3.1 for detail of the GSC). The GSC FoV typically scans a celestial point source for about 60 s in each transit, which is long enough to study X-ray pulsars with several-second pulsations. Thus, the GSC data are useful to study long-term variations of BXPs (e.g., fluxes, periods, and period derivatives).
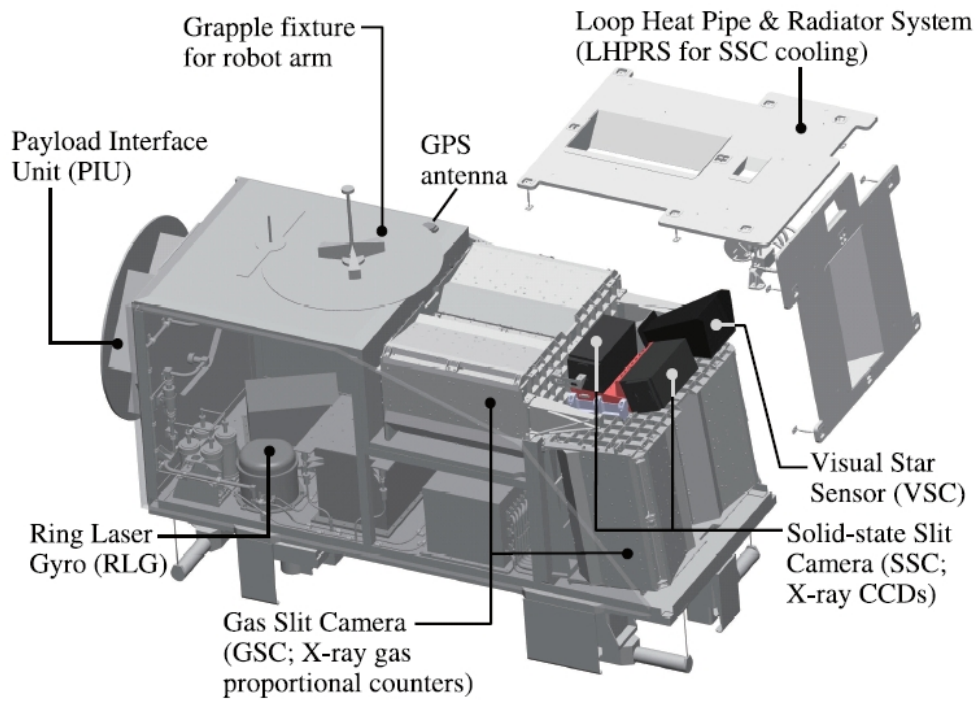
Figure 3.2: An overview of MAXI (Matsuoka et al., 2009).

Table 3.1: The specifications of the GSC (Matsuoka et al., 2009).

| | |
|---|---|
| X-ray detector | 12 pieces of one-dimensional gas proportional counters |
| Composition of gas | Xe (99%) + $CO_2$ (1%) 1.4 atm @ 0 °C |
| X-ray energy range | 2–20 keV |
| Total detection area | 5350 cm$^2$ |
| Energy resolution | 18% (5.9 keV) |
| Field of view | 1°.5 (FWHM) × 160° |
| Slit area for camera unit | 20.1 cm$^2$ |
| Detector position resolution | 1 mm |
| Localization accuracy | 0°.1 |
| Absolute time resolution | 0.1 ms |
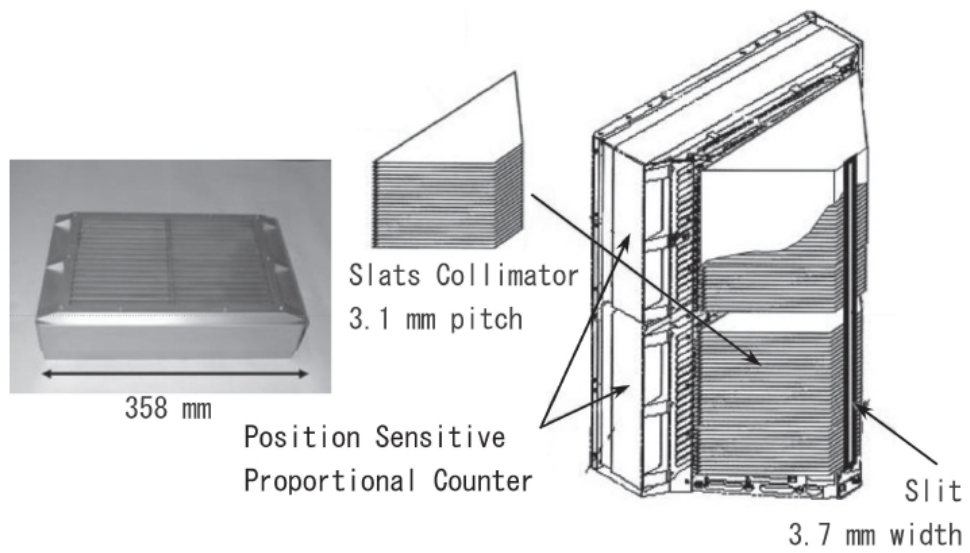
Figure 3.3: A GSC unit (Matsuoka et al., 2009).

# Chapter 4

# OBSERVATIONAL DATA

Since 2009 August, the Gas Slit Camera (GSC), the main instrument of Monitor of All-sky X-ray Image (MAXI) onboard the International Space Station (ISS), has been observing the whole sky in the 2–20 keV band. Every 92 min of the ISS orbital revolution, it scans X-ray point sources each for ~60. Therefore, the GSC allows long-term monitoring of some 100 bright X-ray sources. For these reasons, the GSC data are useful in pursuing fluxes, periods, and period derivatives of BXPs. Although the GSC thus provides one data point every 92 min for a given source, the data are sometimes unavailable; e.g., when the source is dose to the sun, or it is occulted by the ISS solar paddles, or the ISS happens to be in the South Atlantic Anomaly, during the source transit. We should consider these data gaps carefully in data analysis.

## 4.1  MAXI On-demand Process

Although the acquired GSC data are promptly released in the form of 3-band light curves of ~ 400 X-ray sources, these automatically-processed data are not necessarily suited to detailed scientific studies. Instead, we can utilize the MAXI On-demand process system[1], which has been in public since 2011 November. It allows us to produce screened MAXI data for scientific use, including X-ray spectra, light curves and images of any X-ray sources, at any position in the sky and for any time periods since the MAXI started its operation. In this process, users can also define source and background extraction regions by themselves.

---

[1]`http://maxi.riken.jp/mxondem/`

## 4.2    4U 1626–67

The Low-mass X-ray binary pulsar 4U 1626–67, described in § 2.3, is located at $(\alpha, \delta) = (248°.070, -67°.462)$. X-ray spectral analysis was performed using the on-demand GSC data. In timing analysis, we need accurate arrival times of individual X-ray photons. Therefore, for this purpose, we returned to the rawest form of the GSC data, called event data, where the information on individual photons is available. Figure 4.1 shows 4-band light curves of 4U 1626–67, produced from the GSC public data. Thus, the source has been detected at an average intensity of 0.07 c s$^{-1}$ in 2–20 keV. An apparent ~70 day periodicity is caused by precession of the ISS.
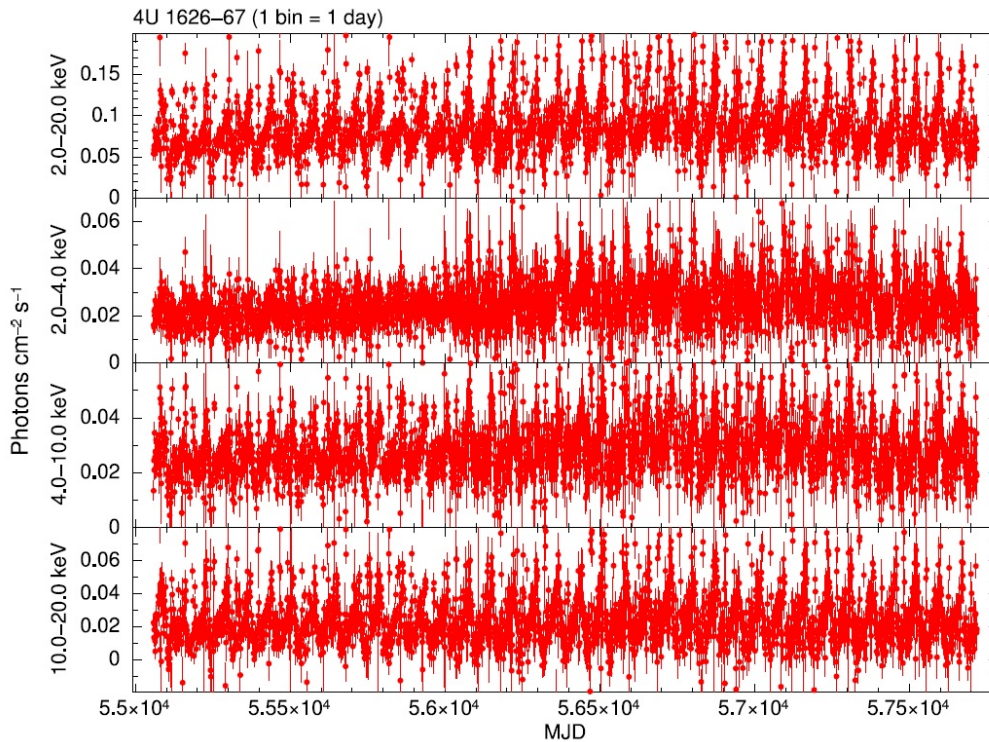


Figure 4.1: Light curves of 4U 1626–67 in the 2–20 keV, 2–4 keV, 4–10 keV and 10–20 keV bands obtained from the MAXI/GSC public data. Each data point represents a 1-day average.

## 4.3    X Persei

The Be X-ray binary pulsar X Persei, introduced in § 2.4, is located at $(\alpha, \delta) = (58°.846, 31°.046)$. We used the data obtained from the MAXI on-demand process

both in timing and spectral analyses. This is because the pulse period of X Persei, ~835 s, is much longer than the individual transit time (~60 s), and hence we do not need to retrieve accurate photon-arrival times. Figure 4.2 shows the same light curves as figure 4.1, but for X Persei. Thus, the 2–20 keV intensity varied by a factor of ~1.2, on time scales of ~1 year.
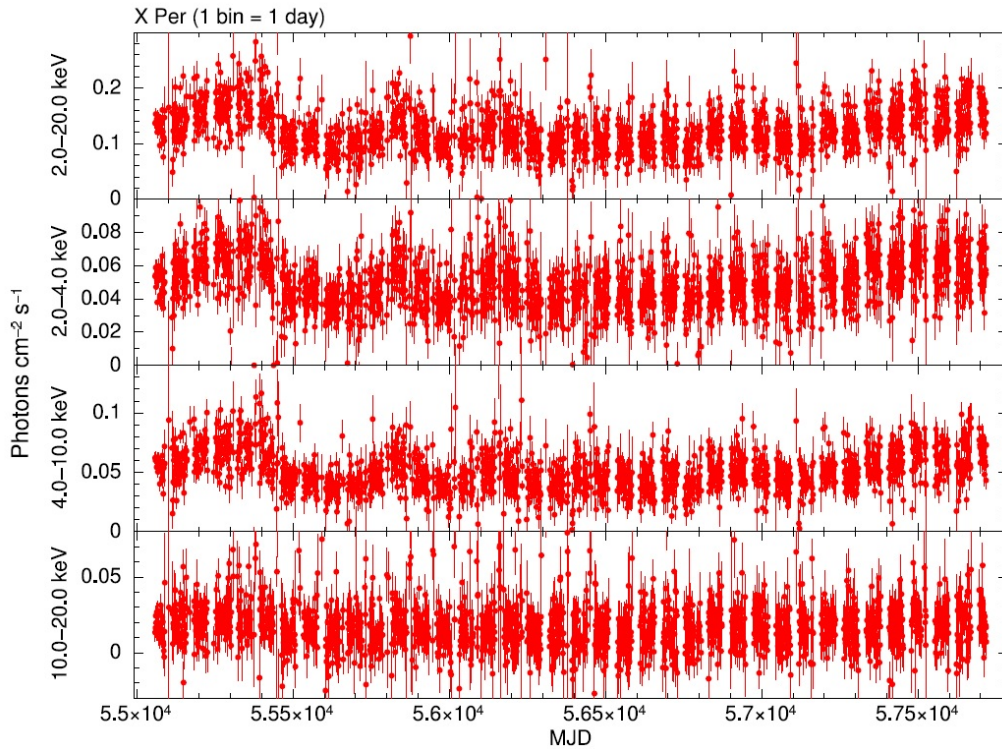


Figure 4.2: The same as figure 4.1, but for X Persei.

# Chapter 5

# DATA ANALYSIS

## 5.1  The Epoch Folding Method

In the timing analysis of this study, we used the epoch folding method in order to derive pulse periods $P$ and pulse-period derivatives $\dot{P}$ of binary X-ray pulsars (BXPs). The epoch folding method is explained as follows.

First, we fold observed data with trial values of $P$ and $\dot{P}$, and obtain a folded light curve. After the calculation of an averaged value of the folded light curve, $\chi^2$ of the folded light curve, defined as

$$\chi^2 \;=\; \sum_{i=1}^{n}\left[\frac{(y_i - \bar{y})}{\sqrt{y_i}}\right]^2 , \; \bar{y} \;=\; \frac{\sum \left(\frac{1}{\sqrt{y_i}}\right)^2 y_i}{\sum \left(\frac{1}{\sqrt{y_i}}\right)^2} , \tag{5.1}$$

where $n$ is the number of bins of the folded light curve and $y_i$ is the number of events in the $i$-th bin, is derived. We search the maximum $\chi^2$ for each trial value of $P$ and $\dot{P}$, and define the $P$ and $\dot{P}$ with the maximum $\chi^2$ as the derived $P$ and $\dot{P}$ in the data. If we fold observed data with the true $P$ and $\dot{P}$, the folded light curve shows the pulse profile of BXPs and gives the maximum $\chi^2$. On the other hand, wrong $P$ and $\dot{P}$ gives a flat folded light curve and a low $\chi^2$, because the light curve is averaged.

## 5.2  4U 1626–67

### 5.2.1  The X-ray light curve with MAXI

We extracted X-ray events of 4U 1626–67 from all-sky GSC data, and accumulated every 60-d interval from MJD 55110 (2009 October 6) to MJD 56550 (2013
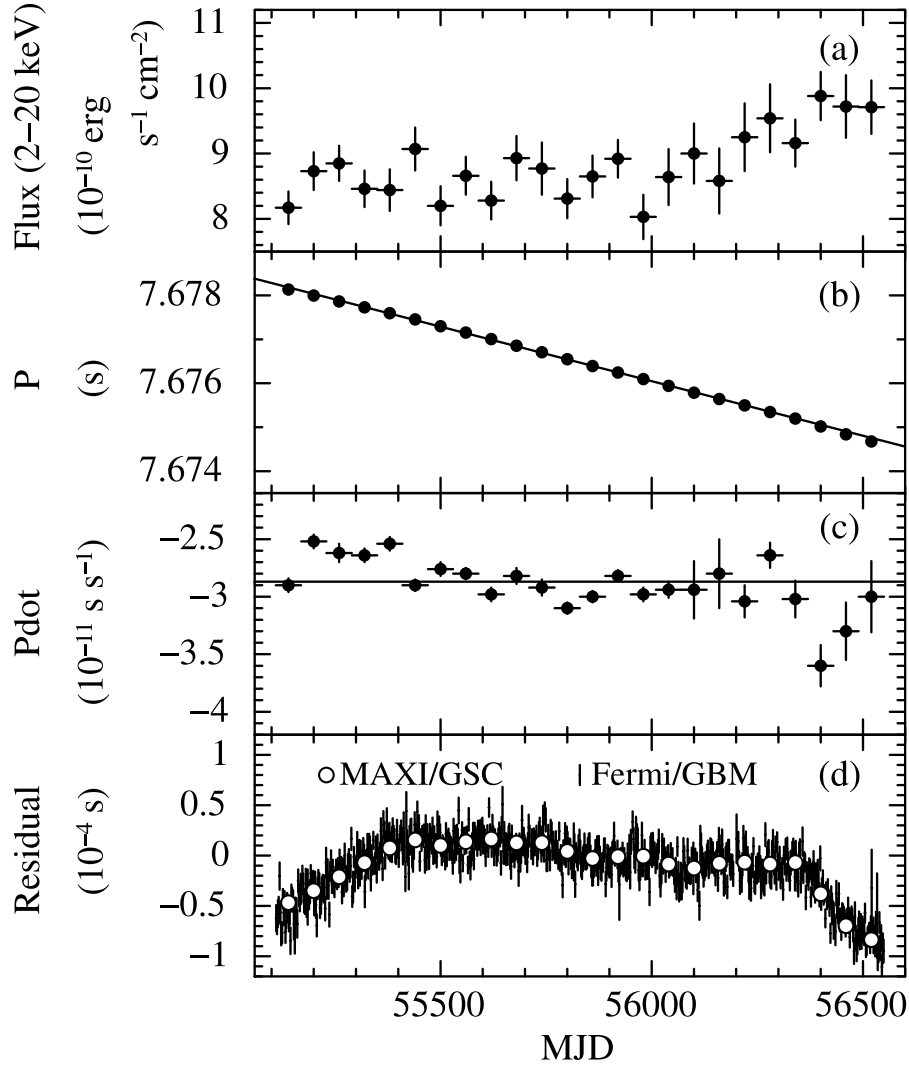
Figure 5.1: The 2–20 keV flux (panel a), the $P$ (panel b), and the $\dot{P}$ (panel c) of 4U 1626–67, obtained from the every 60 d MAXI/GSC data in between 2009 October and 2013 September (Takagi et al., 2016). Panel (d) gives residuals from the best-fit linear function to the period data in (b). The horizontal line in (c) indicates the slope of the line in (b) ($-2.87 \times 10^{-11}$ s s$^{-1}$). The Fermi/GBM results represented by vertical line segments are also plotted.

September 15), using the On-demand process system provided by the MAXI team[1]. To extract the on-source and background events, the following regions were employed: a 2° radius circle for the source region and an annulus with inner and outer radii of 2°.1 and 3°, respectively, for the background region. Figure 5.2 shows these regions and the 2–20 keV image of 4U 1626–67 for MJD 55290–55350. All the obtained spectra were fitted with a power-law model without absorption. The fitting

---

[1]http://maxi.riken.jp/mxondem

results were acceptable for all intervals, and gave photon indices of 1.0–1.3. As an example, in figure 5.3, we show the X-ray spectrum in MJD 55290–55350 with the best-fitting model, which has the photon index of $1.07 \pm 0.05$, the normalization of $(3.5 \pm 0.3) \times 10^{-2}$ and the $\chi^2$ value of 63.6 for 50 degrees of freedom (d.o.f.). We derived the 2–20 keV model fluxes from the results, and plotted in figure 5.1a, where errors are $1\sigma$ statistical uncertainties. The obtained fluxes indicate that the X-ray intensity is almost constant at $\sim 8.6 \times 10^{-10}$ erg cm$^{-2}$ s$^{-1}$ before MJD 56200, and increased to $\sim 9.5 \times 10^{-10}$ erg cm$^{-2}$ s$^{-1}$ after that.
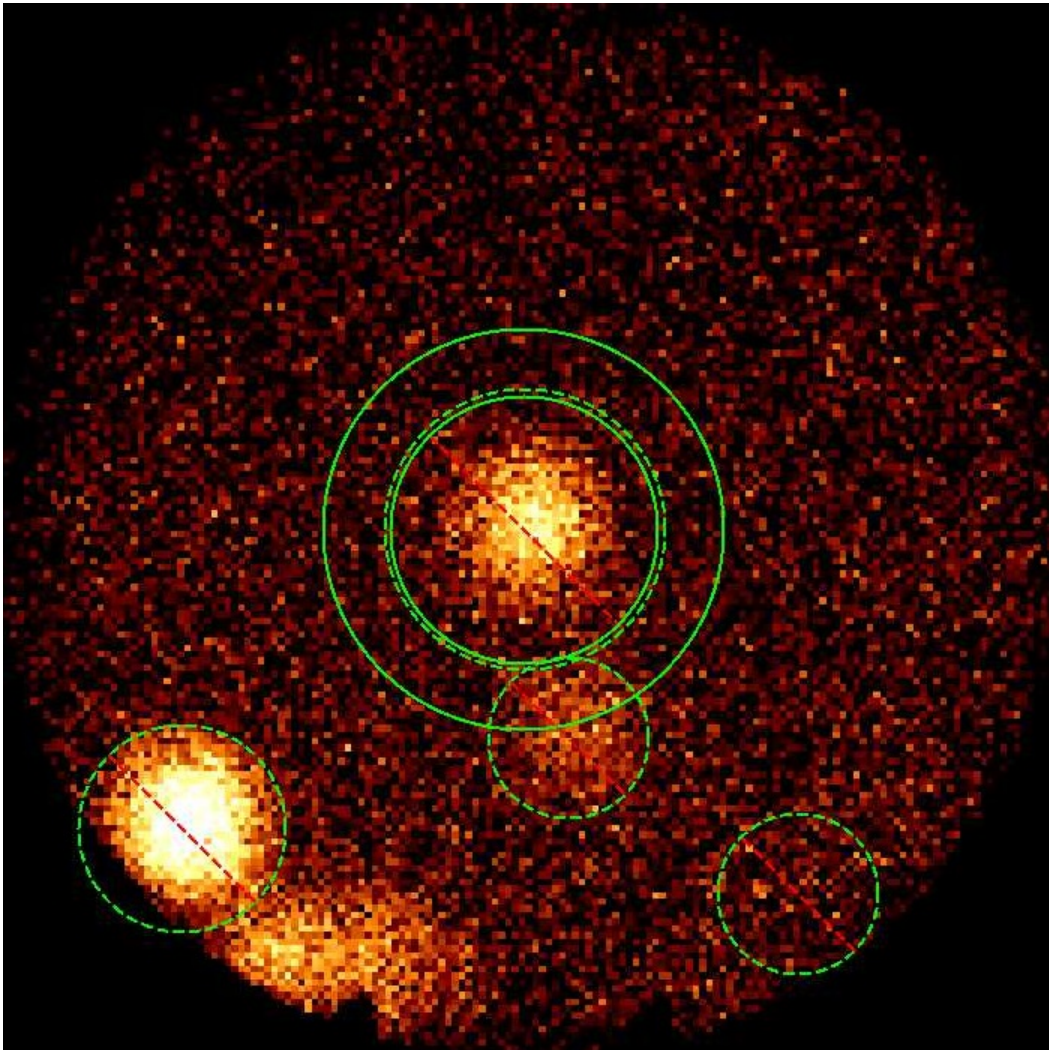


Figure 5.2: The 2–20 keV image of 4U1626–67 obtained from the MAXI/GSC data in MJD 55290–55350. The green solid circles indicate the source and background regions. The green dotted circles express the exclude regions.
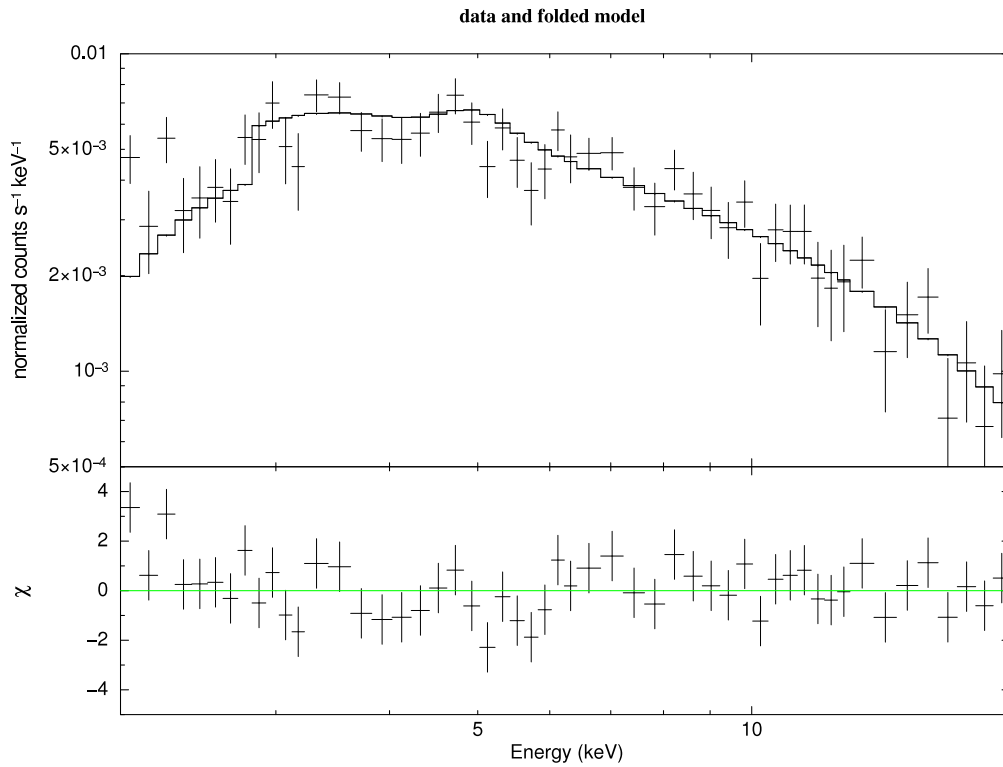
Figure 5.3: The obtained X-ray spectrum of 4U 1626–67 in the 2–20 keV band for MJD 55290–55350. The solid line indicates the best-fitting model with the photon index of $1.07 \pm 0.05$ and the normalization of $(3.5 \pm 0.3) \times 10^{-2}$. The $\chi^2$ value is 63.6 for 50 degrees of freedom.

## 5.2.2 Pulse periods and pulse-period derivatives with MAXI

Using the GSC event data of revision 1.5 with a time resolution of 50 $\mu$s, we performed the pulsar timing analysis of 4U 1626–67. The events were extracted within a $1°.5$ radius from the source position, and then the barycentric correction, which converts a detection time of X-ray photons to that observed at the barycenter of the solar system, was applied to their arrival times. In this analysis, we do not subtracted background events from those events. We derived $P$ and $\dot{P}$ from every 60-d interval data, which is coincident with the light-curve time bins used in § 5.2.1, by using the epoch folding method. We employed $n = 32$, and confirmed that the exposure time of each bin is within $\pm 0.5\%$ from the average values. A search range was selected from the $P$ and $\dot{P}$ values obtained by the Fermi/GBM pulsar project[2], and we assumed that $\dot{P}$ was constant in each interval. As a typical example, we plotted the obtained $\chi^2$ values on the $P$–$\dot{P}$ plane in figure 5.4, employing MJD 55290–55350. The pulse profile in the above span is shown in figure 5.5. We can see a pulse profile

---

[2]http://gammaray.nsstc.nasa.gov/gbm/science/pulsars/lightcurves/4u1626.html

with two sharp peaks, which is the typical pulse profile of 4U 1626–67 in spin-up phases, in figure 5.5. We estimated the 1-$\sigma$ errors of $P$ and $\dot{P}$ with Monte-Carlo simulations (see Appendix A). In order to select the suitable energy band, which gives the highest $\chi^2$, the same analysis was performed for the energy bands of 2–20 keV, 2–10 keV, 2–4 keV, 4–10 keV and 10–20 keV, and we then selected the 2–10 keV band. Results from the other energy bands were consistent with that of the 2–10 keV band.
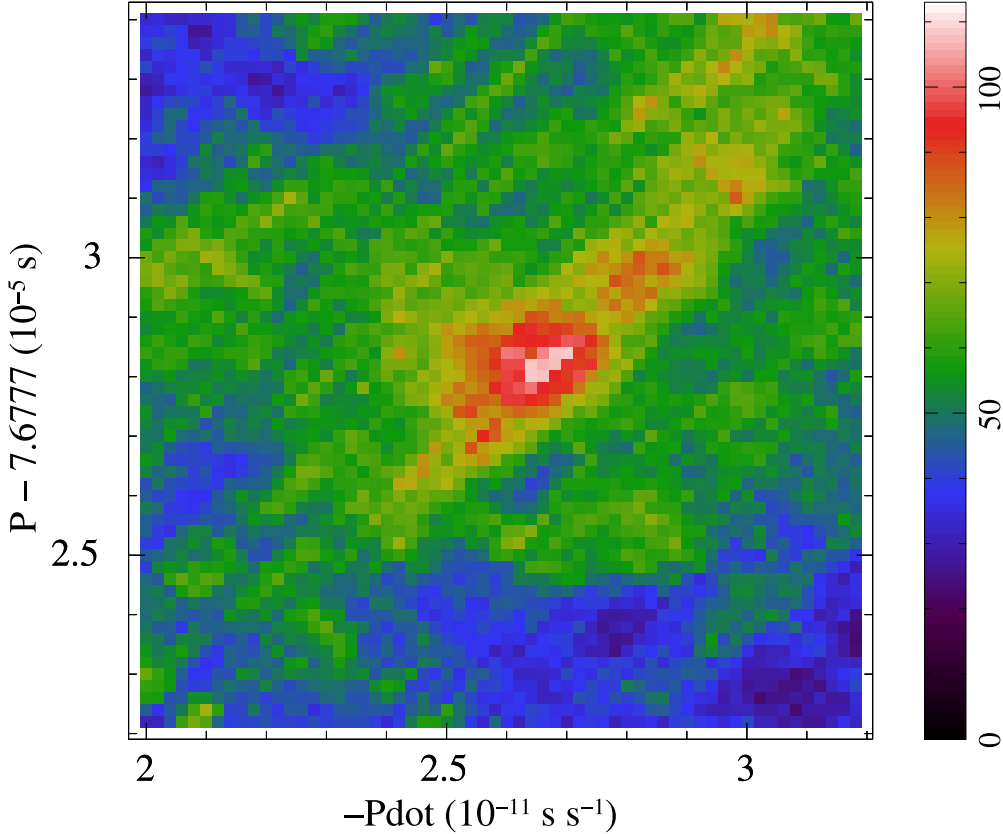


Figure 5.4: Distribution of $\chi^2$ of the folded light curve of 4U 1626–67 obtained from the 2–10 keV MAXI/GSC data in MJD 55290–55350 (Takagi et al., 2016). The right bar indicates the $\chi^2$ values. The maximum $\chi^2$ is 108 for 31 degrees of freedom at $P = 7.6777282$ s and $\dot{P} = -2.64 \times 10^{-11}$ s s$^{-1}$.

Figure 5.1b and 5.1c indicate the obtained $P$ and $\dot{P}$, respectively. The value of $\dot{P}$ was changed and correlated with the flux increase around MJD 56400. We fitted the data points of $P$ in figure 5.1b with a liner function, because their are almost linear. The slope of the best-fit liner function was then derived as $\langle\dot{P}\rangle = -2.87\times10^{-11}$ s s$^{-1}$. We calculated the residuals from the best-fit line, and plotted these in figure 5.1d, where those of the Fermi/GBM pulsar data are also overlaid. The results of the GSC data agree with those of the Fermi/GBM within the errors.
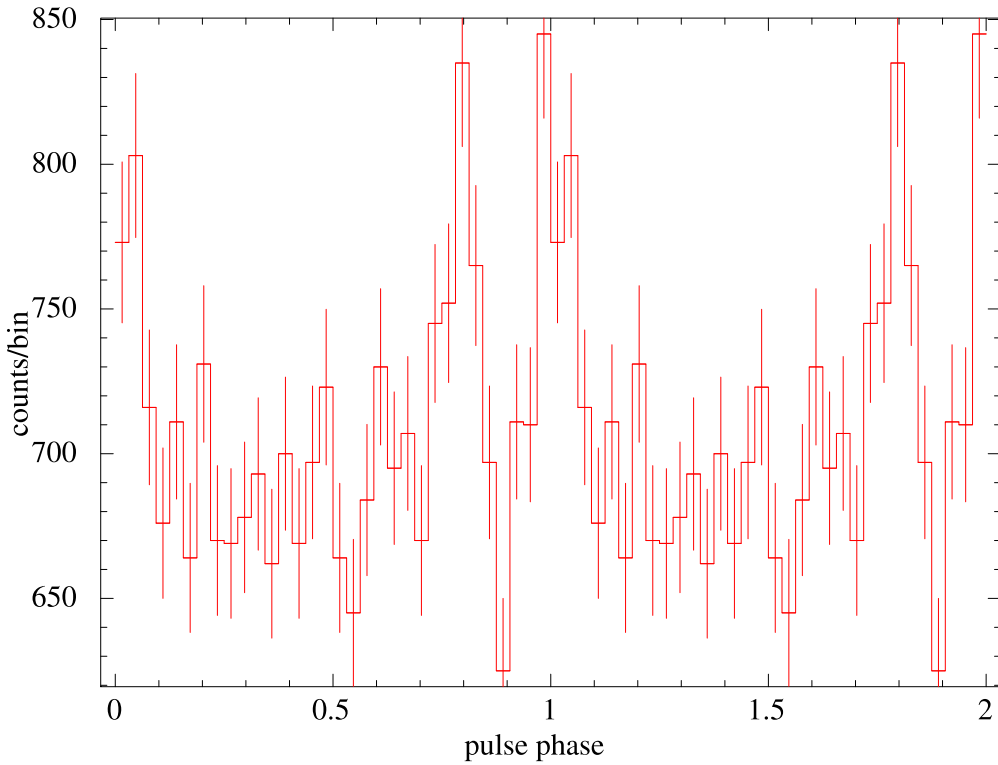
Figure 5.5: The obtained pulse profile of 4U 1626–67, which was folded with $P =$ 7.6777282 s and $\dot{P} = -2.64 \times 10^{-11}$ s s$^{-1}$, in the 2–10 keV band for MJD 55290–55350.

### 5.2.3   An estimation of bolometric fluxes

In the following sections, we apply the accretion torque models, proposed by GL79 and LRB95, to the observed data consisting of those from the previous results and from the GSC data. For this purpose, we have to convert the fluxes of the individual observations to the bolometric fluxes $F_{bol}$, taking account of different energy bands used in different observations, and using spectral models obtained from wide-band X-ray observations.

The energy spectrum of 4U 1626-67 was observed in both the spin-up and spin-down phases (table 2.2 and 2.3), and the changes of the spectral shape between these phases were studied (e.g., Jain et al. (2010); Camero-Arranz et al. (2012)). According to Camero-Arranz et al. (2012), the observed spectra in both phases can be fitted with a model consisting of a blackbody and a cutoff power law, and their difference comes from the blackbody component. The temperature of the spin-up phase and spin-down phase are ~ 0.5 keV and ~ 0.2 keV, respectively. We hence selected these spectral models for the spin-up and spin-down phases, and calculated the fluxes in the 0.5–100 keV band, which are assumed as $F_{bol}$, by using these in

the 2–20 keV band obtained from the GSC data. Since the photon index of a power-law continuum is ∼ 1 below ∼ 20 keV and the exponential cutoff is above ∼ 20 keV, the fluxes below 0.5 keV and above 100 keV are negligible. For example, the conversion factor from the 2–20 keV flux obtained from the GSC data in the spin-up phase to the 0.5–100 keV flux is 1.88. We also applied above calculation to the past observations to derive $F_{bol}$, and indicated the obtained results in table 2.2 and 2.3.

The relation between the observed $\dot{P}$ and the calculated $F_{bol}$, including the past results, are given in figure 6.1. It clearly shows negative correlation, expected from the NS spin up due to the mass accretion.

## 5.3   X Persei
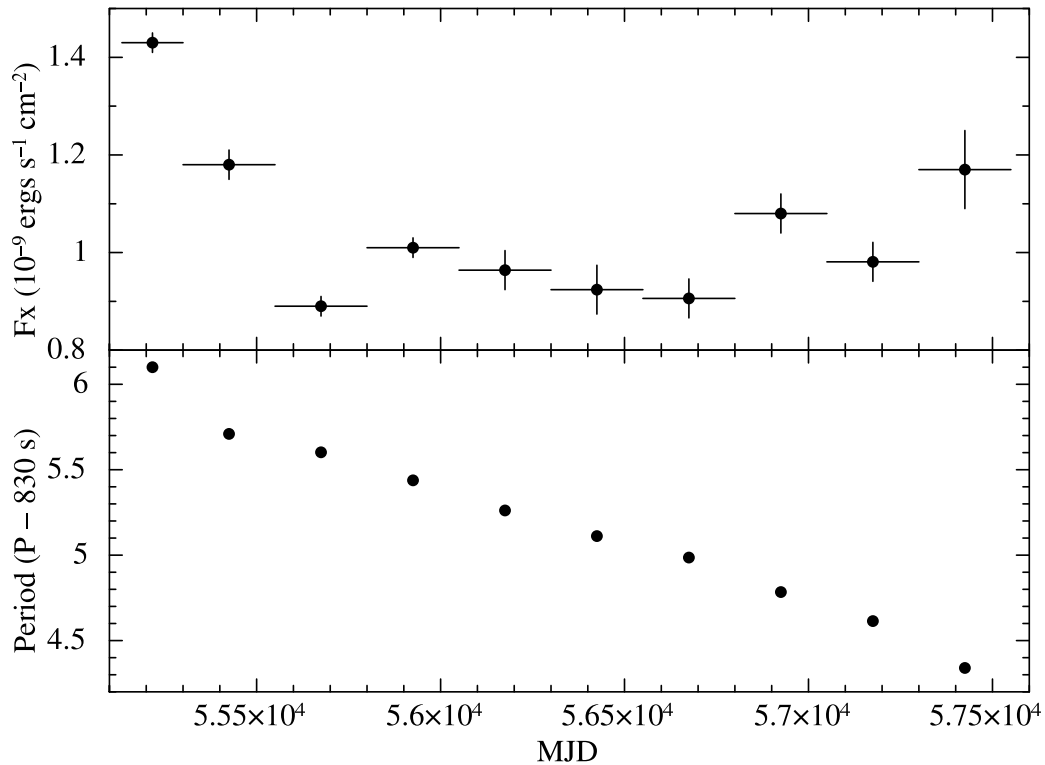


Figure 5.6: The 2–20 keV flux (top) and the $\dot{P}$ (bottom) of X Persei, obtained from the every 250 d MAXI/GSC data between 2009 October and 2016 Jun.

### 5.3.1   The X-ray light curve with MAXI

X-ray events of X Persei were extracted from GSC data, and accumulated every 250-d interval from MJD 55134 (2009 October) to MJD 57550 (2016 Jun), using

the On-demand process system. We employed the following regions to extract the on-source and background events: a $1°.6$ radius circle for the source region and an annulus with inner and outer radii of $1°.7$ and $3°$, respectively, for the background region. Figure 5.7 shows these regions and the 2–20 keV image of X Persei for MJD 55300–55550. The obtained spectra were fitted with a typical model: a power-law component and an exponential cutoff without absorption. The model explained the observed data well, and the results gave photon indices of 0.19–0.45 and cutoff energies of 4.2–5.2 keV. As an example, in figure 5.8, we show the X-ray spectrum in MJD 55300–55550 with the best-fitting model, which has the photon index of $0.22 \pm 0.08$, the cutoff energy of $4.2 \pm 0.3$, the normalization of $(7.3 \pm 0.4) \times 10^{-2}$ and the $\chi^2$ value of 116 for 102 d.o.f.. We calculated the 2–20 keV fluxes from the results, and showed in figure 5.6 (top), where errors are $1\sigma$ statistical uncertainties. The derived fluxes showed that the X-ray intensity changed from $\sim 14 \times 10^{-10}$ erg cm$^{-2}$ s$^{-1}$ to $\sim 9 \times 10^{-10}$ erg cm$^{-2}$ s$^{-1}$ in MJD 55134–55800. While the intensity is almost constant in MJD 55800–56800, it increased to $\sim 12 \times 10^{-10}$ erg cm$^{-2}$ s$^{-1}$ after MJD 56800.

### 5.3.2 Pulse periods with MAXI

In the timing analysis of X Persei, we used light curves in 1 scan bin, in which events in ~60 s, corresponding to 1 scan transit of a point source, were accumulated. These are obtained from the On-demand process system, because we were not able to derive $P$ from the GSC event data due to variabilities of background. Since background is subtracted in the On-demand process system, we can avoid that effect. We employed the same regions in § 5.3.1 to obtain the light curves, and the 2–20 keV band. The heliocentric correction, which converts a detection time of photons to that observed at the center of the sun, and binary orbit correction, which converts a time of X-ray emission from a NS to that at the center of the NS orbit, assuming a circular orbit, were applied to the light curves. We derived $P$ from every 250-d interval data by using the epoch folding method, and then employed $n = 32$. A search range was selected from the results of past observations, and we assumed that $\dot{P}$ is constant in each interval. As a typical example, we plotted the obtained $\chi^2$ values on the $P$–$\dot{P}$ plane in figure 5.9, employing MJD 55300–55550. The pulse profile in the above span is shown in figure 5.10. We can see a pulse profile with a sinusoidal shape, which is the typical pulse profile of X Persei. We calculated the 1-$\sigma$ errors of $P$ from a method proposed by Leahy (1987). The obtained $P$ is plotted in figure 5.6 (bottom). Although we derived the values of $\dot{P}$ by the epoch folding
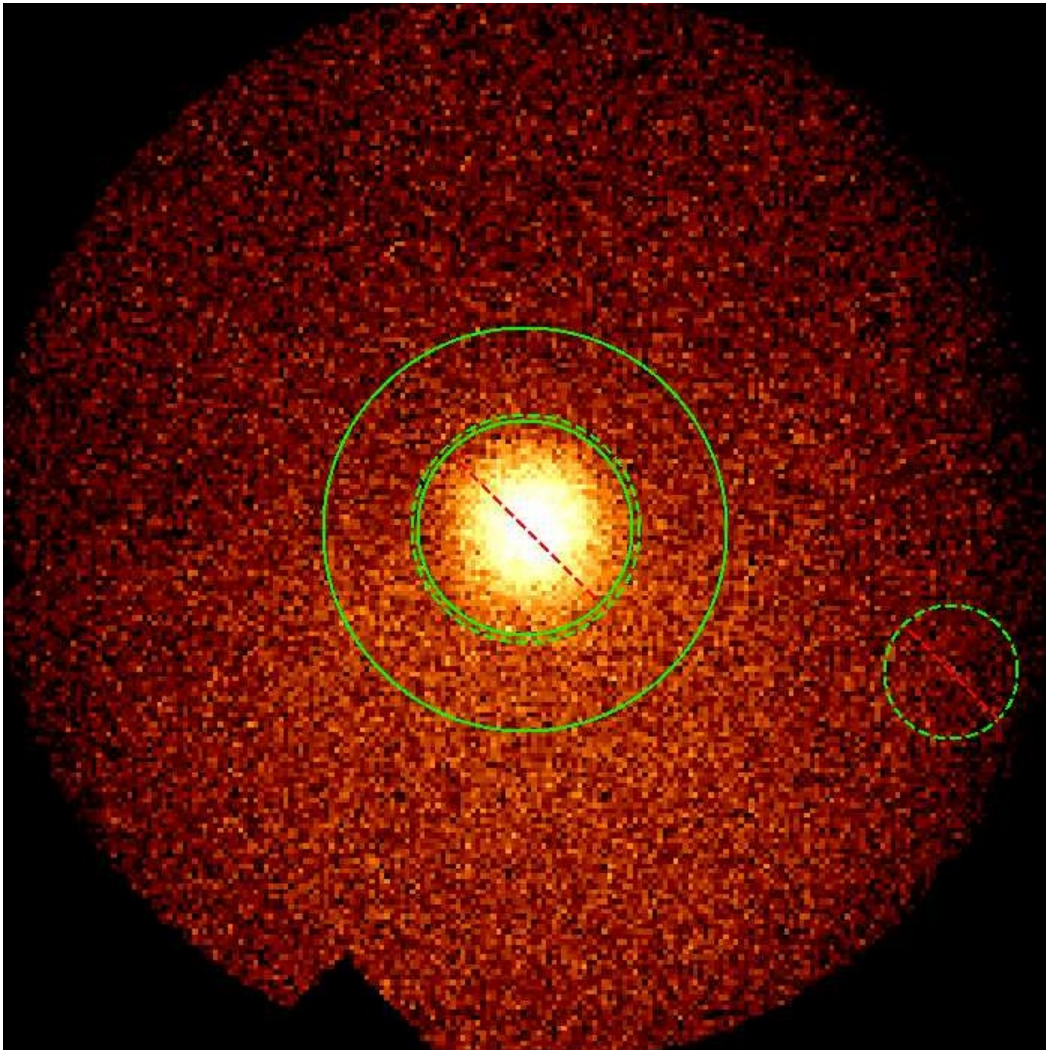
Figure 5.7: The 2–20 keV image of X Persei obtained from the MAXI/GSC data in MJD 55300–55550. The green solid circles indicate the source and background regions. The green dotted circles express the exclude regions.

method, $\dot{P}$ was calculated from the difference between two points of $P$ because the obtained $\dot{P}$ has a large uncertainty.

### 5.3.3   An estimation of bolometric fluxes

Lutovinov et al. (2012) performed spectral analysis of X Persei with data obtained with RXTE/PCA, which include both spin-up and spin-down phases, and fitted the obtained spectra in the 2–20keV band with a model consisting of an interstellar absorption, power law and blackbody components. They, then, showed that there is
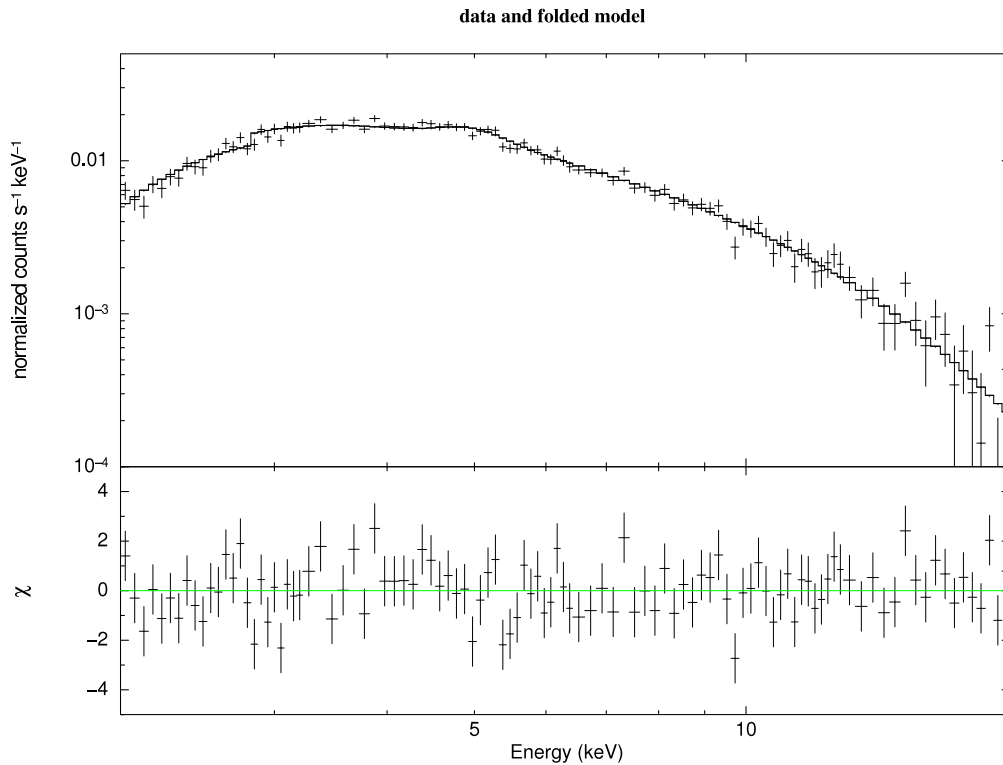
Figure 5.8: The obtained X-ray spectrum of X Persei in the 2–20 keV band for MJD 55300–55550. The solid line indicates the best-fitting model with the photon index of $0.22 \pm 0.08$, the cutoff energy of $4.2 \pm 0.3$, the normalization of $(7.3 \pm 0.4) \times 10^{-2}$. The $\chi^2$ value is 116 for 102 degrees of freedom.

no big difference of the parameters between spin-up and spin-down phases except for the normalization factor. Di Salvo et al. (1998) analyzed the energy spectrum of X Persei in the 0.1–200 keV band obtained from BeppoSAX in 1996 September corresponding to the spin-down phase, and obtained the spectral model. Although they did not give a model in the spin-up phase, we employed the obtained spectral model to convert the observed flux to the bolometric flux for both the spin-up and spin-down phases. The conversion factor from the 2–20 keV flux to the 0.1–200 keV flux is 1.81. We also applied the correction to the past observations. The relation between the observed $\dot{P}$ and the calculated $F_{\mathrm{bol}}$ is shown in figure 6.5. Although data points in figure 6.5 are a little scattered, it shows negative correlation.
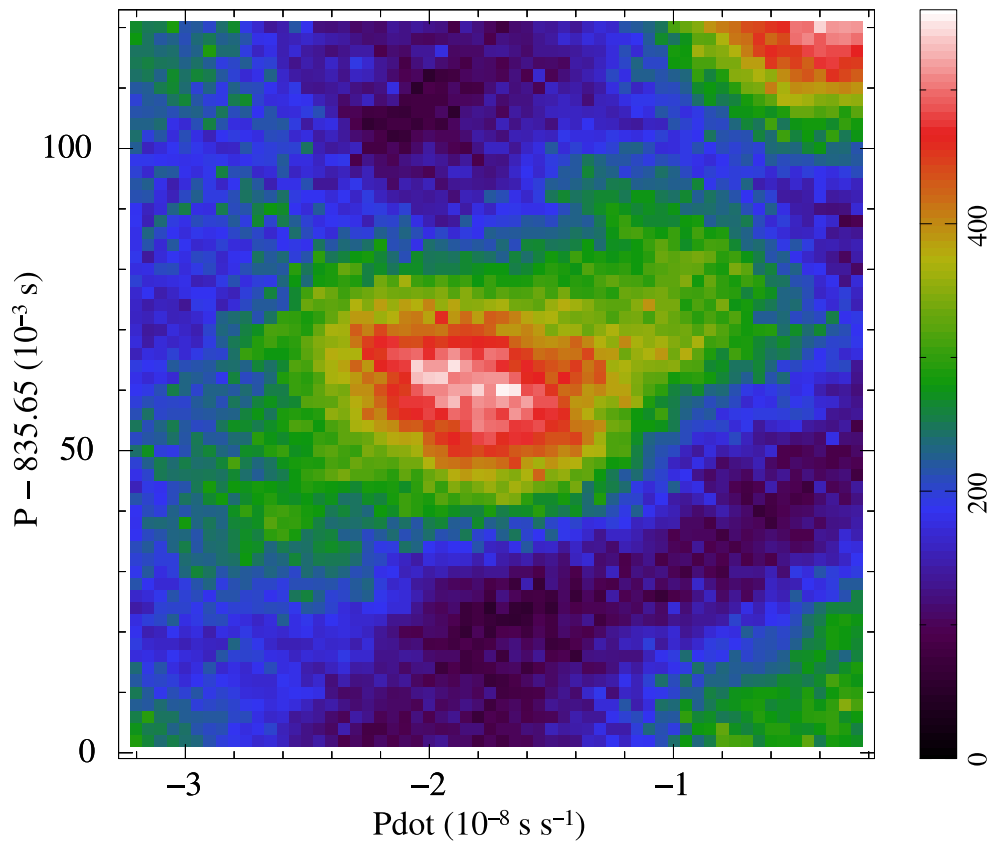
Figure 5.9: Distribution of $\chi^2$ of the folded light curve of X Persei obtained from the 2–20 keV MAXI/GSC data in MJD 55300–55550. The right bar indicates the $\chi^2$ values. The maximum $\chi^2$ is 555 for 31 degrees of freedom at $P = 835.71$ s and $\dot{P} = -1.70 \times 10^{-8}$ s s$^{-1}$.
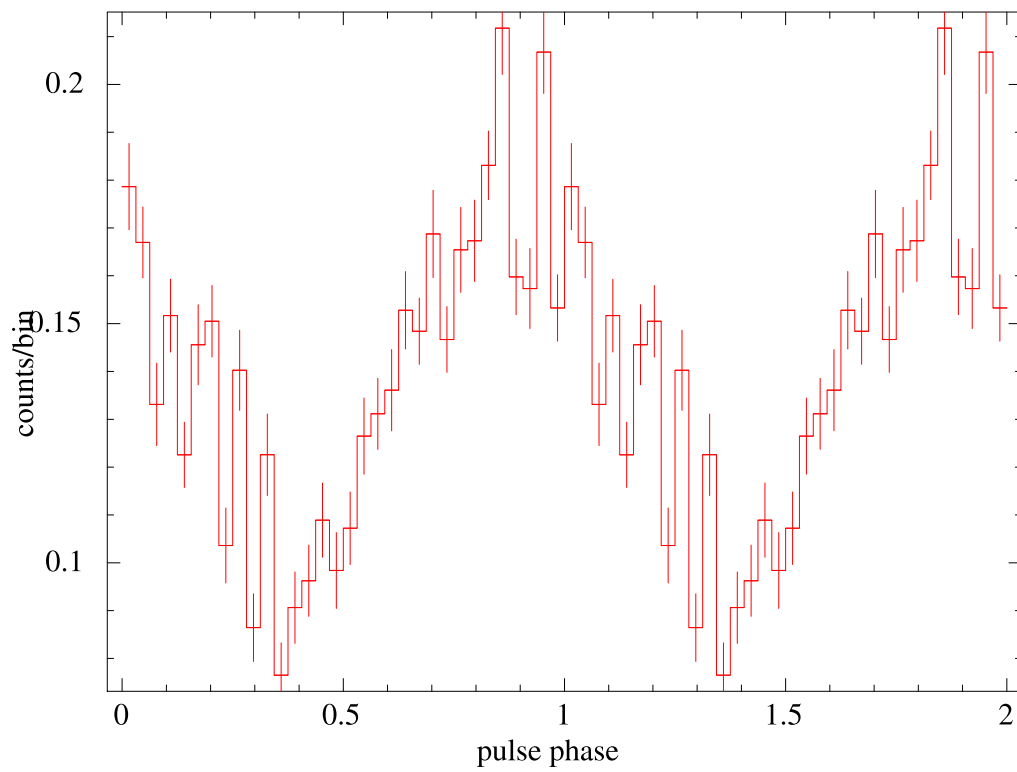
Figure 5.10: The obtained pulse profile of X Persei, which was folded with $P = 835.71$ s and $\dot{P} = -1.70 \times 10^{-8}$ s s$^{-1}$, in the 2–20 keV band for MJD 55300–55550.

# Chapter 6

# RESULTS

## 6.1 4U 1626–67

### 6.1.1 Model equations relating $\dot{P}$ to the flux

As reviewed in § 2.2.3, GL79 assumed that the accreting matter transfers its angular momentum to the neutron star (NS) at the "outer transition zone", $r_0$ [equation (2.25)], and proposed a relation between $\dot{P}$ and $L$ in binary X-ray pulsars (BXPs). It is very similar to an earlier work by Rappaport & Joss (1977). Although their equation contains an unknown parameter ($\xi v_{\mathrm{r}}/v_{\mathrm{ff}}$), its relation to their overall model is calculable. Therefore, we employed the equation proposed by GL79.

According to GL79, $\dot{P}$ is described by equation (2.26). There, $S_1(M)$ includes the moment of inertia $I$, which is expressed as a function of $M$ and $R$. Since $I$ also depends on the EoS, we used its approximation proposed by Lattimer & Schutz (2005),

$$I \simeq (0.237 \pm 0.008) \, MR^2 \left[ 1 + 0.42 \left( \frac{M}{M_\odot} \right) \left( \frac{R}{10 \ \mathrm{km}} \right)^{-1} + 0.009 \left( \frac{M}{M_\odot} \right)^4 \left( \frac{R}{10 \ \mathrm{km}} \right)^{-4} \right],$$

$$(6.1)$$

which is utilized in most of the major EoS models for $M/R \gtrsim 0.07 M_\odot \ \mathrm{km}^{-1}$.

In 4U 1626–67, the value of $B$ is accurately known from the CRSF (§ 2.1.1) as $B = 3.2 \times 10^{12} \, (1 + z_{\mathrm{g}}) \ \mathrm{G}$, and is considered to be the magnetic field strength near the magnetic poles. GL79 assumed that the magnetic axis is aligned to the NS rotation axis, and used the equation of $\mu$ at the equator described by

$$\mu = \frac{1}{2} BR^3.$$

$$(6.2)$$

Since equation (6.2) does not include relativistic effects, we employed the equation considering that effect,

$$\mu = \frac{BR^3}{2}\frac{X^3}{3}\left[-\ln(1-X) - X - \frac{X^2}{2}\right]^{-1}, \quad X = \frac{2GM}{Rc^2} = \left(\frac{R}{R_S}\right)^{-1}, \quad (6.3)$$

to calculate $\mu$ more accurately, where $R_S$ is the Schwarzschild radius (Wasserman & Shapiro, 1983).

When the emission from an NS is isotropic, its $L$ is estimated from $F_{bol}$ and the source distance $D$ as

$$L = 4\pi D^2 F_{bol}. \quad (6.4)$$

Since the emission is generally anisotropic, the equation is not exactly correct. We use this approximation, and then evaluate the effect in a later section. In order to calculate $L$ including the relativistic effects, we also employed the equation,

$$L = c^2 \dot{M}\left[1 - (1-X)^{-\frac{1}{2}}\right], \quad (6.5)$$

described by Wasserman & Shapiro (1983).

By using equations (2.26), (6.1), (6.3), and (6.5), as well as the description for $z_g$ [equation (2.16)], we derived a theoretical equation, which includes three unknown parameters, $D$, $M$ and $R$, to express the observed $\dot{P}$–$L$ relation as

$$\dot{P} = -5.8 \times 10^{-10} \mu_{30}^{\frac{2}{7}} n(\omega_s) R_6^{\frac{6}{7}} \left(\frac{M}{M_\odot}\right)^{-\frac{3}{7}} I_{45}^{-1} P^2 L_{37}^{\frac{6}{7}} \text{ s s}^{-1}. \quad (6.6)$$

## 6.1.2   Application of the Ghosh & Lamb relation to the data

To derive the possible parameter ranges of $D$, $M$ and $R$ of 4U 1626–67, we fitted the obtained $\dot{P}$–$F_{bol}$ relation in figure 6.1 with equation (6.6). When some past measurements do not have the associated errors of $\dot{P}$, we added an arbitrarily small value ($\Delta\dot{P} = 6 \times 10^{-16}$ s s$^{-1}$) to them. Since the errors of $F_{bol}$ are dominant in the obtained data, this effect was confirmed to little affect the fitting results. Because the observed $\dot{P}$–$F_{bol}$ relation cannot simultaneously constrain the three parameters, we assumed the source distance $D$ to be in a range from 3 to 20 kpc, and then calculated the allowed $M$–$R$ regions for each assumed distance. For example, figure 6.1 shows the fitting result when assuming $D = 8$ kpc. In this case, we have obtained the best fit values of $M = 1.34M_\odot$ and $R = 11.6$ km (the errors are considered later).

In order to understand how the theoretical curve depends on $M$ and $R$, we show
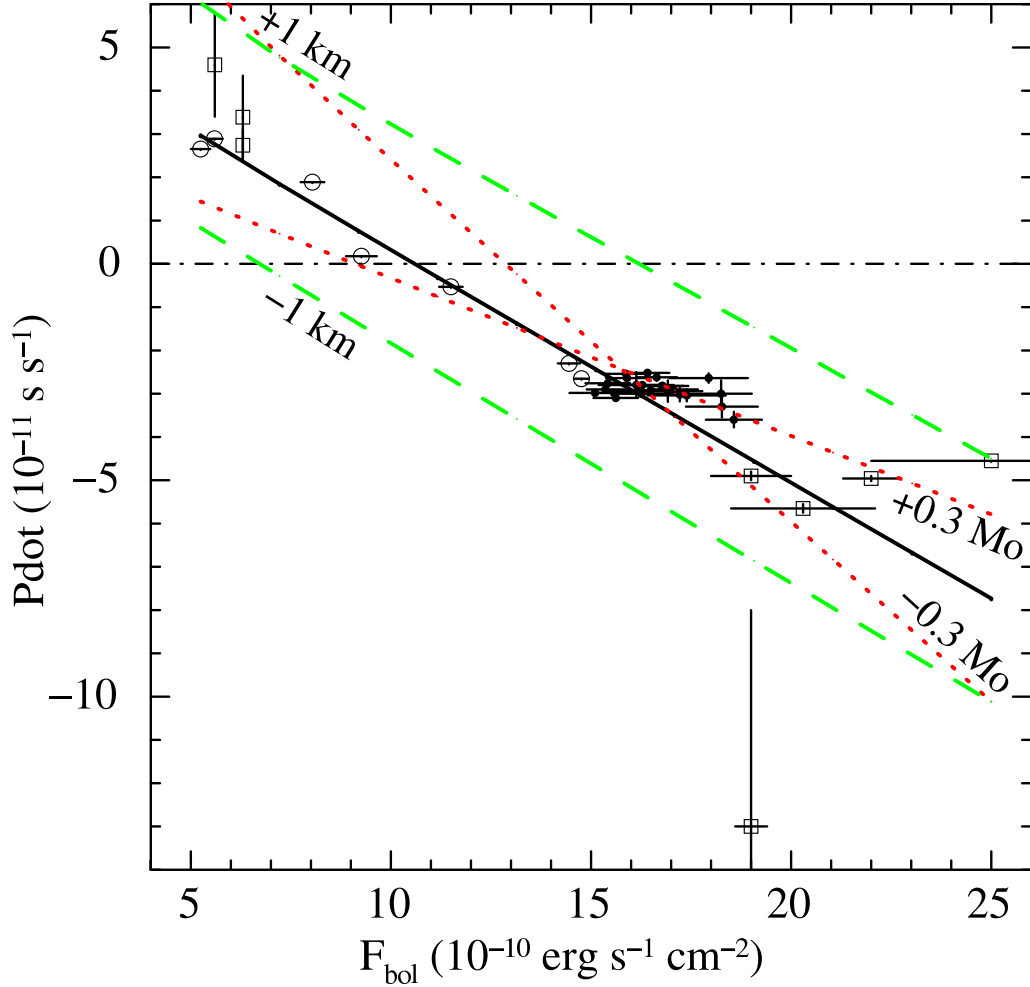
Figure 6.1: A relation between $\dot{P}$ and $F_{bol}$ by the MAXI/GSC and past observations of 4U 1626–67. Filled circles, open circles and squares represent the MAXI/GSC data, the Swift/BAT data and the others in table 2.2 and 2.3, respectively. The dashed-dotted horizontal line indicates $\dot{P} = 0$. The solid line is the best fit model calculated from equation (6.6) proposed by GL79, assuming a distance of 8 kpc. The parameters are $M = 1.34 M_\odot$ and $R = 11.6$ km, with $\chi_\nu^2$ of 2.9 for 37 degrees of freedom. Dashed two lines show the case when $R$ is changed by $\pm 1$ km with $M$ kept unchanged, while dotted two lines those when $M$ is varied by $\pm 0.3 M_\odot$ with $R$ fixed at 11.6 km. This figure was updated from Takagi et al. (2016).

in figure 6.1 the curves predicted by the GL79 relation, in which either $M$ or $R$ is slightly changed. When $R$ was changed with $D$ and $M$ fixed, the theoretical curve shifted in parallel, with little changes in its slope. On the other hand, a change of $M$, with $D$ and $R$ fixed, gave a change of the slope of the theoretical curve. In other words, the observed $\dot{P}$–$F_{bol}$ relation can determine $R$ and $M$ simultaneously (if $D$ is given), from the zero-cross point and the $\dot{P}$–$F_{bol}$ slope, respectively. Below, let us

consider physical meanings of this mechanism.

In figure 6.1, the zero-cross point represents a torque-equilibrium condition, where the co-rotation radius of equation (2.33), which is almost uniquely determined by $P$ with some dependence on $M$, becomes equal to the outer-transition radius $r_0$ of equation (2.25). At this radius, the gas pressure estimated from $L \propto D^2 F_{\mathrm{bol}}$ balances the magnetic pressure, and this condition allow us to estimate the value of $\mu$. By comparing the obtained $\mu$ with $B$ measured from the CRSF, we can derive $R$ via equation (6.2) or (6.3). As a result, the zero-cross point is more sensitive to $R$ rather than $M$. To be more quantitative, equation (2.30) in the torque-equilibrium condition, in which it becomes 0.349, can be combined with equation (6.2) or (6.3), to yield

$$F_{\mathrm{bol}} \propto M^{-\frac{2}{3}} R^5 D^{-2}, \tag{6.7}$$

where dependences on $B$ and $P$ were omitted. Thus, the zero-cross point value of $F_{\mathrm{bol}}$ is very sensitive to $R$.

The slope of the $\dot{P}$–$F_{\mathrm{bol}}$ relation in figure 6.1 expresses the dependence of the NS rotation change on the luminosity, which is proportional to the accretion rate. Since the rotation change depends on $I$, which is a function of $M$, an increase of $M$ gives a smaller slope. An increase of $R$ also produces the same scenario through $I$, but the effect is partially canceled by changes of $\mu$ in equation (6.6) when $B$ is fixed. As a result, the change of the slope mainly depends on $M$. We can describe quantitatively in the following way. In the higher spin-up region which accurately determines the slope, we can approximate $\omega_{\mathrm{s}} \to 0$. Then, $n(\omega_{\mathrm{s}})$ becomes constant from figure 2.6, and we can rewrite equation (6.6) as

$$-\dot{P} \propto M^{-\frac{10}{7}} R^{-\frac{2}{7}} L^{\frac{6}{7}} \propto M^{-\frac{10}{7}} R^{-\frac{2}{7}} D^{\frac{12}{7}} F_{\mathrm{bol}}^{\frac{6}{7}}, \tag{6.8}$$

when the higher-order terms in equation (6.1) are ignored. From the above equation, the slope is described as

$$-\frac{d\dot{P}}{dF_{\mathrm{bol}}} \propto M^{-\frac{10}{7}} R^{-\frac{2}{7}} D^{\frac{12}{7}} F_{\mathrm{bol}}^{-\frac{1}{7}}. \tag{6.9}$$

Thus, the slope depends mainly on $M$, rather than on $R$.

We derived the best-fit $M$ and $R$ when $D$ was assumed, and present the solutions as a solid line in figure 6.2. The $M$–$R$ relation in figure 6.2 can be analytically obtained as follows. When a value of $D$ is assumed, the bolometric flux at zero-point gives $M^{-2/3} R^5 D^{-2}$ via equation (6.7), while the slope in figure 6.1 gives

$M^{-10/7}R^{-2/7}D^{12/7}F_{\text{bol}}^{-1/7}$ via equation (6.9). By eliminating $D$ from these equations, and ignoring the weakly varying factor $F_{\text{bol}}^{-1/7}$, we obtain

$$M \propto R^2 \tag{6.10}$$

which roughly explains the locus in figure 6.2. The $M$–$R$ relations from a few representative EoSs, SLy (Douchin & Haensel, 2001), APR (Akmal et al., 1998), and Shen (Shen et al. (1998a); Shen et al. (1998b)), all taken from Yagi & Yunes (2013) are also shown in the figure 6.2.

So far, $D$ has been treated as an unconstrained parameter. However, we may require the obtained $M$ and $R$ to be in their nominal ranges, $M = (1.0 - 2.4)\,M_\odot$ and $R = 8.5 - 15$ km (e.g. Bhattacharyya (2010); Özel (2013)). Then, the distance is constrained as $D = 6 - 14$ kpc, which is consistent with the result by Chakrabarty (1998).

In figure 6.1, the best-fit reduced chi-squared, $\chi_\nu^2 = 2.9$ for $\nu = 37$ d.o.f., means that the fit is not acceptable. One possible reason for the large $\chi^2$ is systematic errors on the observed fluxes, because the fluxes taken from various past observations must suffer from cross-calibration uncertainties among the different instruments. We hence added various systematic errors on the flux, and found that $\chi_\nu^2 \sim 1$ is achieved if we employ systematic errors of 5.5%. This value is considered to be reasonable, because it is in the uncertainty range ($\sim 10\%$) of the fluxes obtained from different instruments as estimated by Kirsch et al. (2005). Since the fitting results gave that $\chi_\nu^2$ depend little on $D$, we have employed the systematic error of 5.5%, and derived the 68% confidence limits ($\chi^2$ increment $\Delta\chi^2 < 2.3$ for 2 d.o.f.), which include only the statistically errors. In figure 6.2, the obtained statistical errors are expressed by a pair of dashed lines.

### 6.1.3   Systematic uncertainties

Although the fitting with the GL79 model has given a rather tight constraints on $M$ and $R$ for an assumed value of $D$, the uncertainty region in figure 6.2 (dashed lines) includes only statistical errors. Therefore, we have to evaluate systematic errors arising from approximations and several assumptions which we are involved in the GL79 formalism as well as in our analysis. Accuracy of the approximations of equation (2.28) for $n(\omega_s)$ in the GL79 model, and equation (6.1) for $I$, are considered to be within $< 5\%$ (GL79) and $< 10\%$ (Lattimer & Schutz, 2005), respectively. Since these uncertainties are considered to be smaller than following uncertainties,

we ignored these effects, and evaluated other systematic errors.

An obvious uncertainty arise from the assumption of the isotropic emission from the NS; so far, we assumed that the observed time-averaged flux is equivalent to the averaged one over the whole direction of the NS rotation. Although the uncertainty involved in this assumption has not been evaluated in 4U 1626–67, Basko & Sunyaev (1975) estimated that the effect is at most 50% in a similar low-mass X-ray binary pulsar Her X-1. Assuming that the result can be applied to 4U 1626–67 as well, we set the systematic uncertainty on the observed flux to be $\sim$ 50%, which directly affects the estimated $L$ in equation (6.6). Another uncertainty in the present study is the accretion geometry assumed by GL79, which includes the exact location of the "outer transition zone" described by $r_0$ of equation (2.25), and the angles among the rotation axis of the NS, the NS's magnetic axis, and the accretion plane. In the GL79 model, they assumed that the rotation axis is aligned with the magnetic axis, and these axes are perpendicular to the accretion plane. If these assumptions do not hold, $\mu_{30}$ will change, typically by $\sim$50% (Wasserman & Shapiro, 1983). Because $r_0 \propto \mu_{30}^{4/7}$ and equation (6.6) scales as $\propto \mu_{30}^{2/7}$, the 50% uncertainty in $\mu_{30}$ will translate to a geometrical uncertainty of $\sim$25% in equation (6.6).

In order to express all the above uncertainties, we have decided to employ an artificial normalization factor $A$, and multiplied it to the right hand side of equation (6.6). Then, we repeated the model fitting with changing $A$ from 0.5 to 1.5. In figure 6.2, the obtained $M$–$R$ loci for $A = 0.5$, 0.8, 1.2, and 1.5 are also shown. Although these uncertainties make the allowed $M$–$R$ region wider, the GL79 model still gives a very tight constraint on $R$ if $D$ is somehow specified.

## 6.1.4 Application of the Lovelace model to the data

As introduced in § 2.2.4, LRB95 proposed another (in a sense more sophisticated) accretion torque model, Lovelace model hereafter, to describe the relation between $\dot{P}$ and $L$ with assumptions of magnetic outflows and/or magnetic breaking. Using the "turnover radius" $r_{to}$ [equation (2.32)] and the co-rotation radius $r_{cr}$ [equation (2.33)], the Lovelace model explains spin-up with outflows when $r_{to} < r_{cr}$, and predicts both spin-up and spin-down behavior with magnetic braking by the disk when $r_{to} > r_{cr}$. In order to understand both the spin-up and spin-down behavior of 4U 1626–67 with the Lovelace model, the model requires the condition of $r_{to} > r_{cr}$ in the spin-down phase. However, in the spin-down phase of 4U 1626–67, we found that the parameters, which we employed, do not give the condition of $r_{to} > r_{cr}$. Specifically, we obtained the values of $r_{to} = 1.3 \times 10^8$ cm and $r_{cr} = 7.0 \times 10^8$ cm
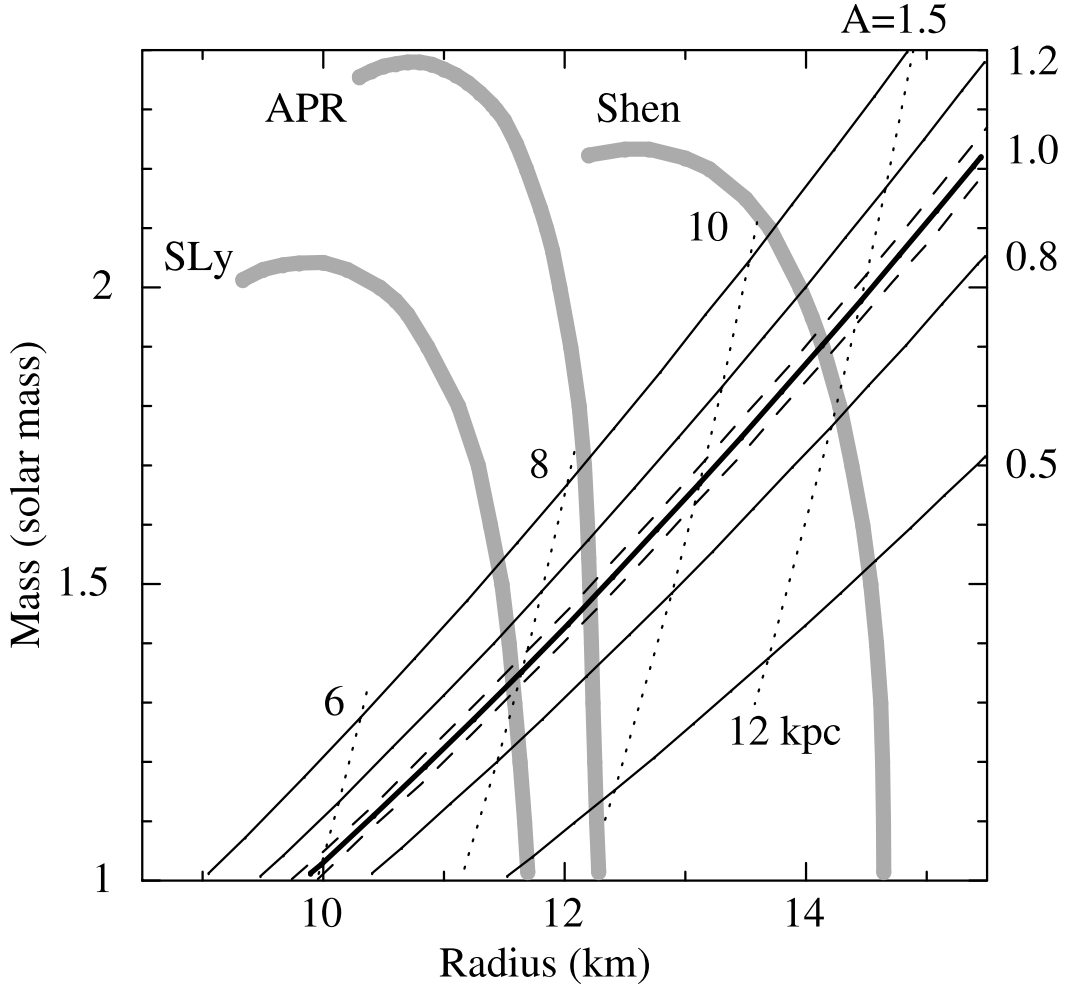
Figure 6.2: Results of the GL79 model fits to the data of 4U 1626–67, shown on the *M–R* plane. The thick solid line indicates a locus of the best-fit values of *M* and *R* as *D* is varied. The thin solid lines express the cases of four different values of the normalization factor *A*. A pair of dashed lines give 68% errors for the solutions of *A* = 1.0, while dotted lines give a grid of constant values of *D*. The gray solid lines represent *M–R* relations given by the EoSs of SLy, APR and Shen. This figure was updated from Takagi et al. (2016).

from $F_{bol}$ = 9.3 × $10^{-10}$ erg cm$^{-2}$ s$^{-1}$, $M$ = $1.73M_\odot$, $R$ = 11.1 km, $D$ = 6 kpc, and $\alpha D_m$ = 0.01. Therefore, we found that the Lovelace model cannot explain the spin-down behavior of 4U 1626–67.

Although the Lovelace model does not satisfy the required condition in the spin-down phase, we applied the model to the observed data in the spin-up phase, because $r_{to} < r_{cr}$ is satisfied there in. We then should use the equation in the spin-up with outflows proposed by LRB95, which expresses the $\dot{P}$–$L$ relation as equation 2.35. In LRB95, they assumed that $\alpha$ is in the range of 0.01–0.1 and $D_m$ is order of unity.

While equations (2.35) and (6.6) have different factors, $\alpha D_{\mathrm{m}}$ and $n(\omega_{\mathrm{s}})$, the other factors in the equations are the same.

We thus selected the data in the spin-up phase from tables 2.2 and 2.3, and fitted them with equation (2.35), employing the parameter ranges of $M = 1.0 - 2.4 M_{\odot}$ and $R = 8.5 - 15$ km. In this analysis, we did not consider the relativistic effect in $\mu$ or $L$. A fitting result with an assumed distance of $D = 6$ kpc and $\alpha D_{\mathrm{m}} = 0.01$ is shown in figure 6.3, in the same format as figure 6.2 (but limited to $\dot{P} < 0$). The obtained reduced chi-squared, $\chi_{\nu}^{2} = 46$ for 30 d.o.f., indicates that the fitting result is far from being acceptable. Even if we change $D$ or $\alpha D_{\mathrm{m}}$, the fit was not improved significantly. The result is expected, because equation (2.35) can only take $\dot{P} = 0$, which is a torque-equilibrium condition, with $F_{\mathrm{bol}} = 0$. The Lovelace model differs on this point from that of GL79, and disagrees with our measurements. From these results, we concluded that the accretion torque model proposed by LRB95 cannot explain the relation observed from 4U 1626–67.

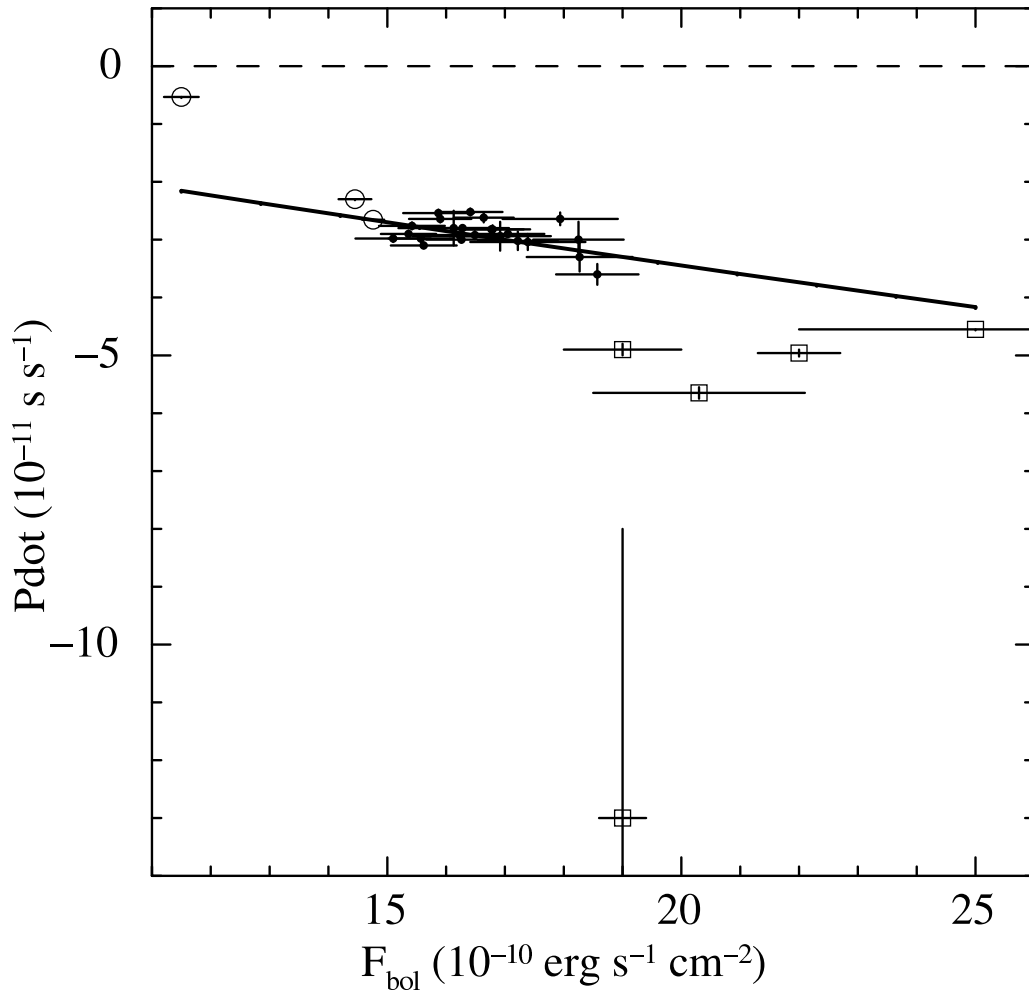Figure 6.3: The same as figure 6.1, but employing the Lovelace model (LRB95) (Takagi et al., 2016). The dashed horizontal line gives $\dot{P} = 0$. The solid line indicates the best fit model calculated from equation (2.35) proposed by LRB95 with $M = 1.73 M_\odot$, $R = 11.1$ km, $D = 6$ kpc, and $\alpha D_{\mathrm{m}} = 0.01$. The obtained reduced chi-squared is $\chi_\nu^2 = 46$ (1400/30) for 30 d.o.f..

## 6.2 X Persei

### 6.2.1 Past observations

In order to study X Persei (§2.4) in the same way as in § 6.1, we combined the GSC result with the past observations summarized in table 6.1. Figure 6.4 shows the $\dot{P}$ and $F_{\mathrm{bol}}$ relation of X Persei obtained from the GSC and the past results. Although we observe a negative correlation, the trend of the GSC data is different from that of the past observations. This suggest that the GL79 theory is somehow inapplicable to X Persei, or some of the employed data are wrong. We speculate that the latter is the case, because the correlation will become much better if the three RXTE/PCA data points by Acuner et al. (2014) are moved in the flux direction by a factor of ~2. In the following section, we therefore reanalyze the past results obtained by Acuner et al. (2014), trying to solve the problem.

### 6.2.2 Re-analysis of the RXTE/PCA data

Although the 3–20 keV RXTE/PCA flux reported by Acuner et al. (2014) in their figure 5 corresponds to ~18 mCrab at ~MJD 52500, the RXTE/ASM intensity obtained by Lutovinov et al. (2012) is ~25 mCrab at that time. The source intensity calculated from the RXTE/PCA count rate given in figure 1 in Acuner et al. (2014) in reality translates to is ~30 mCrab instead of ~18 mCrab. In contrast, the GSC data points in figure 6.4 are considered correct, because the spectrum analysis and the photon count rate (figure 4.2) gave consistent results. Therefore, we concluded that the RXTE/PCA flux calculated by Acuner et al. (2014) is wrong.

We have hence decided to employ reanalyzed RXTE/PCA fluxes derived by M. Nakajima (2016, private communication), which are also summarized in table 6.1. Thus, the RXTE/PCA fluxes have increased by a factor of 1.8–2.1, just as we speculated. By using there revised flux values, Then, we obtained the $\dot{P}$ and $F_{\mathrm{bol}}$ relation, figure 6.4 has changed in to figure 6.5. Now, most of the data points define a single correlation.
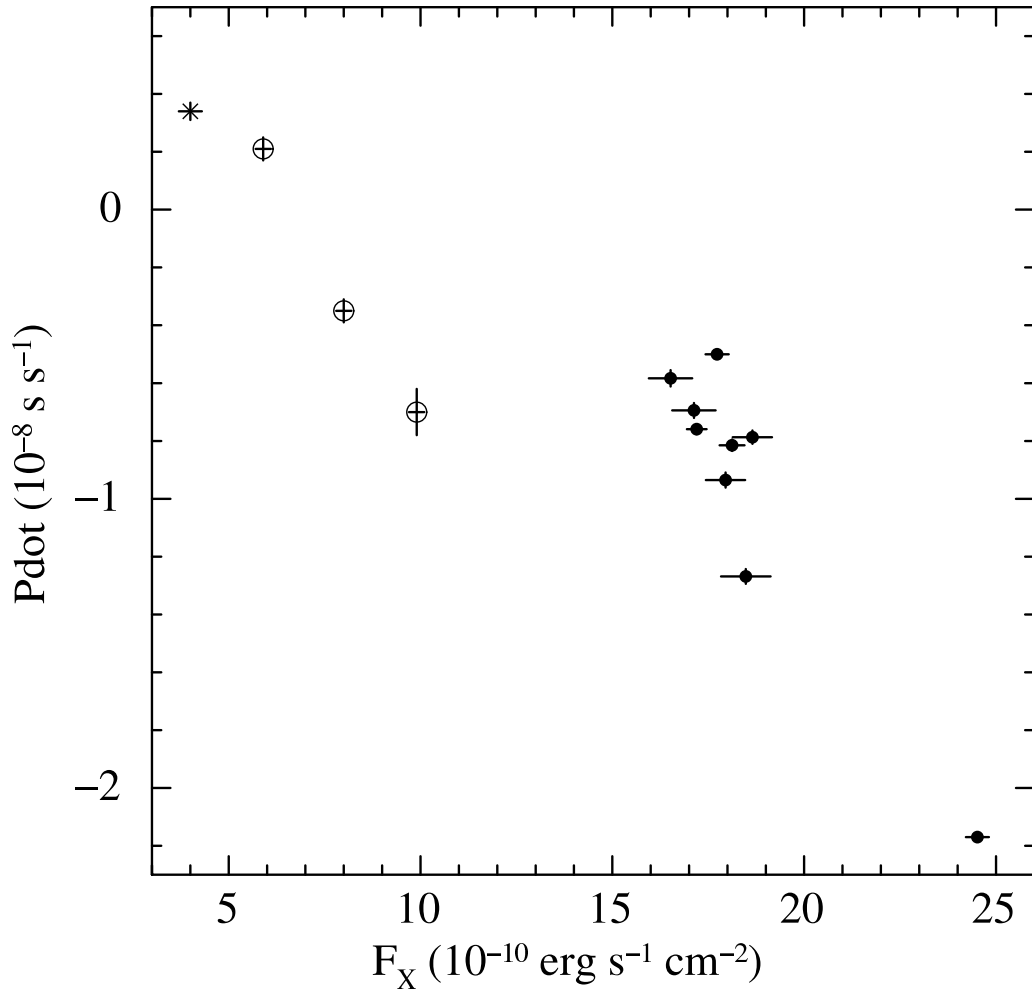
Figure 6.4: A relation between $\dot{P}$ and $F_{bol}$ of X Persei obtained by the MAXI/GSC and the past observations. Filled circles, open circles and a cross represent the MAXI/GSC, the RXTE/PCA (Acuner et al., 2014) and the BeppoSAX (Di Salvo et al., 1998) data summarized in table 6.1, respectively.

Table 6.1: X-ray flux and period derivative obtained in past observations of X Persei.

| Observation | Flux | | | | Pulsation | | Ref.[3] |
| Date | Period (MJD) | Band (keV) | Obs. ($10^{-10}$ erg s$^{-1}$ cm$^{-2}$) | Bolometric[1] ($10^{-10}$ erg s$^{-1}$ cm$^{-2}$) | Epoch (MJD) | $\dot{P}$ ($10^{-9}$ s s$^{-1}$) | |
|---|---|---|---|---|---|---|---|
| 1996 Sep | 50335–50338 | 0.1–200 | $4.0 \pm 0.3$ | $4.0 \pm 0.3$ | ~50000 | $3.4 \pm 0.3^3$ | (1) |
| 2001 Jul | 52105 | 3–20 | $2.8 \pm 0.1$ | $5.9 \pm 0.2$ | 52105 | $2.1 \pm 0.4$ | (2) |
| 2001 Jul | ~52105 | 3–20 | $4.94 \pm 0.03^4$ | $10.37 \pm 0.07$ | | | (3) |
| 2002 Jan | 52285 | 3–20 | $3.8 \pm 0.1$ | $8.0 \pm 0.2$ | 52285 | $-3.5 \pm 0.4$ | (2) |
| 2002 Jan | ~52285 | 3–20 | $6.91 \pm 0.02^4$ | $14.51 \pm 0.05$ | | | (3) |
| 2002 Sep | 52525 | 3–20 | $4.7 \pm 0.1$ | $9.9 \pm 0.2$ | 52525 | $-7.0 \pm 0.8$ | (2) |
| 2002 Sep | ~52525 | 3–20 | $10.0 \pm 0.1^4$ | $20.9 \pm 0.2$ | | | (3) |

All errors represent 1-$\sigma$ uncertainties.

[1] Converted 0.1–200 keV flux, assuming the spectral models in Di Salvo et al. (1998).

[2] (1) Di Salvo et al. (1998) (BeppoSAX), (2) The data were taken from figure 5 in Acuner et al. (2014) (RXTE/PCA), (3) An average flux calculated from the fluxes obtained by M. Nakajima (2016, private communication) (RXTE/PCA).

[3] Averaged value.

[4] Revised RXTE/PCA flux.

### 6.2.3   Application of the Ghosh & Lamb relation to the data

In order to derive the possible NS parameters in X Persei, $M$, $R$ and $B$, we fitted the obtained $\dot{P}$–$F_{bol}$ relation in figure 6.5, with the GL79 theory of equation (6.6). In X Persei, the number of unknown parameters in the equations is four, $M$, $R$, $D$, and $B$, whereas the data have only two degrees of freedom, the zero-cross point and the slope, as we confirmed in §6.1.2. Therefore, we tried to estimate only $B$, while the other parameters are allowed to take arbitrary values in reasonable ranges of $M = (1.0 - 2.4)\ M_{\odot}$, $R = 8.5 - 15$ km, and $D = 0.7 - 1.3$ kpc. For example, figure 6.5 shows a fitting result with $M = 1.7 M_{\odot}$, $R = 13.7$ km, $D = 0.7$ kpc, and $B = 5 \times 10^{13}$ G. Although the data points are a little scatted, the theoretical curve roughly explains the observed data.

To derive the preferred range of $B$ in X Persei, we repeated the same analysis by changing $B$. The obtained best-fit $\chi^2$ values are shown in figure 6.6 as a function of $B$. Thus, the fit is clearly much better for $B = (4 - 20) \times 10^{13}$ G, where the $\chi^2$ value is constant due to degenerate solutions with different values of $M$, $R$, and $D$. As indicated by a green line in figure 6.5, the model fails to explain the data if $B$ is higher than this range, and require the limiting value of $R = 8.5$ km trying to reduce $\mu$ via equation (6.2). Similarly, values of $B$ less than $4 \times 10^{13}$ G (red line in figure 6.5) disagree with the data, and require the largest value of $R = 15.5$ km for the same reason as above. Thus, the range of $B = (4 - 20) \times 10^{13}$ G is clearly preferred in X Persei, although the obtained minimum $\chi^2$ value of 427 for 11 d.o.f. is still far from being acceptable. In this fitting, we did not consider the uncertainties of the model equations.

In obtaining figure 6.5, we have assumed for simplicity $D = 0.7$ kpc. However, due to the degeneracy of solutions, the same fit as the black line in figure 6.5 can be obtained even for different values of $D$. If, for example, we employ $D = 0.8$ kpc, the best-fit solution can be reproduced by $M = 1.9 M_{\odot}$ and $R = 14.7$ km. In any case, our conclusion on $B$ does not change.
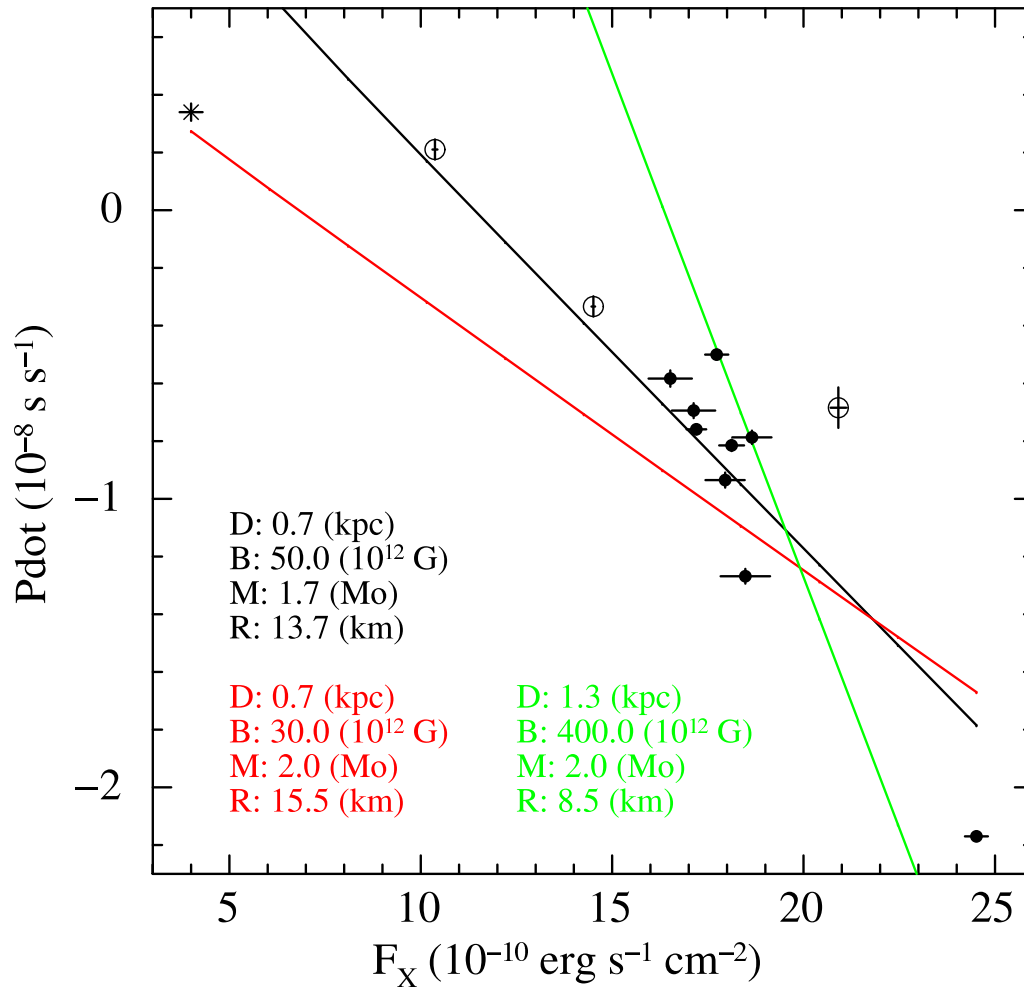
Figure 6.5: The same as figure 6.4, but the flux values of the three RXTE/PCA data points have been revised (table 6.1). The black solid line is the best fit GL79 model of equation (6.6), which has $M = 1.7 M_\odot$, $R = 13.7$ km and $B = 5.0 \times 10^{13}$ G, assuming a distance of 0.7 kpc. The red and green solid lines indicate the fitting models with $B = 3.0 \times 10^{13}$ G and $B = 4.0 \times 10^{14}$ G, respectively. The parameters in those models are described in this figure, where their colors correspond to those of the models.
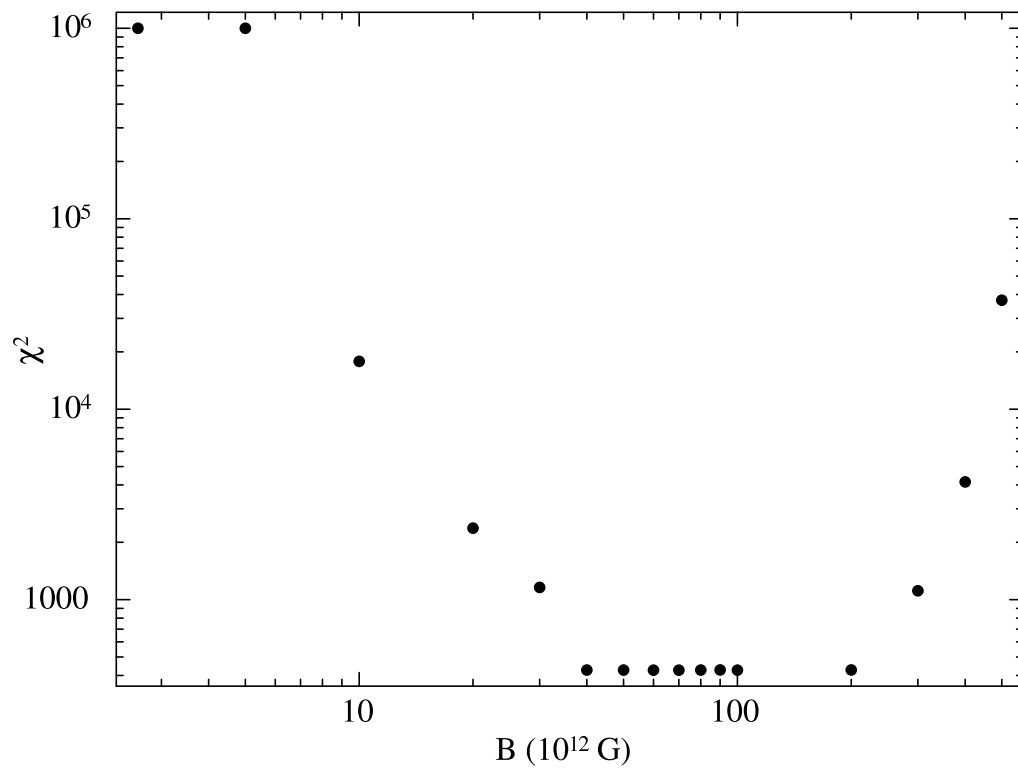
Figure 6.6: Dependence of $\chi^2$ on the assumed $B$, obtained when fitting the observed data of X Persei in figure 6.5 with equation (6.6).

# Chapter 7

# DISCUSSION

## 7.1 A Mass and Radius of the Neutron Star in 4U 1626–67

We applied the epoch folding method to the data of 4U 1626–67 observed with the GSC, and then determined $P$, $\dot{P}$, and the X-ray intensity of 4U 1626–67 for every 60-d interval from 2009 October to 2013 September. The obtained results indicate that the NS in 4U 1626–67 has been in spin-up phase since the start time of the GSC operation, and the values of the spin-up rate were correlated with the X-ray intensity.

As shown in figure (6.1), we confirmed that these GSC results were fully consistent with those obtained from the past observations summarized in table 2.2 and 2.3. The observed data in both spin-up and spin-down phases shows good correlation of $\dot{P}$–$F_{bol}$, and the change rate is $\dot{P} = -6 \times 10^{-11}$ s s$^{-1}$ in the spin-up phase, and $\dot{P} = 5 \times 10^{-11}$ s s$^{-1}$ in the spin-down phase. The past observations include the transitions between the spin-up and spin-down phases. By using the favorable conditions, we found that the accretion torque model proposed by GL79 successfully explains the relation between $\dot{P}$ and $F_{bol}$ observed in 4U 1626–67, while the model proposed by LRB95 cannot explain the observed relation even limiting to the spin-up phase.

Another favorable condition is the accurate knowledge of the surface magnetic field of the NS in 4U 1626–67. We found that the two unknown parameters, e.g., $M$, $R$ and $D$, can be constrained when the observed $\dot{P}$–$F_{bol}$ relation was fitted with the accretion torque model proposed by GL79. The source distance can be constrained to $D = 6 - 14$ kpc under the condition that $M$ and $R$ are limited to the nominal ranges of $M$ and $R$ of NSs, $M = (1.0 - 2.4)\,M_\odot$ and $R = 8.5 - 15$ km. This result is agree with the limit $D \gtrsim 3$ kpc calculated by Chakrabarty et al. (1997); they analyzed

the behavior of $\dot{P}$ in 4U 1626–67 with the assumption of $I = 1 \times 10^{45}$ g cm$^2$ and $M = 1.4\ M_\odot$, then evaluated the mass accretion rate, $\dot{M} \gtrsim 1 \times 10^{16}$ g s$^{-1}$, using a similar consideration to the GL79 model, and compared the calculated luminosity to the observed flux. Our result of the distance estimation also agrees with that by Chakrabarty (1998), 5–13 kpc, which was obtained from the optical intensity and assumption that the effective X-ray albedo of the accretion disk is $\gtrsim 0.9$.

In other words, if we assume the source distance $D$, the observed $\dot{P}$–$F_{\mathrm{bol}}$ relation can constrain $M$ and $R$ simultaneously with small statistical errors. Thus, if other measurements can determine $D$ accurate enough, the allowed $M$ and $R$ region of 4U 1626–67 can be constrained to a narrow range, which is considered to be able to select the unique EoS. Moreover, the method can give the information on $R$, which is more important than that on $M$, when the obtained result suffer from various systematic errors (figure 6.2).

To increase the accuracy of the GL79 model, it is important to evaluate the systematic errors discussed in § 6.1.3. An application of the GL79 model to Be X-ray binaries by Klus et al. (2014) should help to understand the uncertainties. They compared the surface magnetic field of NSs in these binaries obtained from CRSF ($B_{\mathrm{C}}$) with that calculated by the GL79 model ($B_{\mathrm{GL79}}$), and found that the ratio is $B_{\mathrm{GL79}}/B_{\mathrm{C}} = 3-4$ in two systems, GRO J1008–57 and A0535+26. The derived ratio corresponds to an uncertainty of ~50%, which is equivalent to $A = 1.5$ evaluated in § 6.1.3. These results require that it is important to apply this method to many sources.

# 7.2   A Magnetic Field of the Neutron Star in X Persei

By using the same method in 4U 1626-67, we tried to estimate the surface magnetic field of the NS in X Persei, and found that the referred range is $B = (4 - 20) \times 10^{13}$ G. However, in this estimation, we did not consider the uncertainties of the model equations and evaluate the errors of $B$. Although the result includes the above problem, it is consistent with a suggestion that the NS in X Persei has a strong magnetic field (Sasano, 2015). On the other hand, Lutovinov et al. (2012) indicated an absorption feature in the X-ray spectrum observed with INTEGRAL, and estimated the value of $B = (2.4-2.9) \times 10^{12}$ G with assumption that the feature is CRSF. The feature is very shallow and broad, and may arise from wrong continuum modeling because it disappear using another continuum model. From these results, we considered that the NS in X Persei has strong magnetic field ($\sim 10^{13}$ G) which

is stronger than that of a NS in general binary X-ray pulsars.

# Chapter 8

# CONCLUSIONS

In present study, we have found the below conclusions.

- Application of the accretion torque model proposed by Ghosh & Lamb (1979) to the observed relation between $\dot{P}$ and $F_{\mathrm{bol}}$ can constrain the mass and radius of the neutron star simultaneously with small statistical errors, which can select the unique equation of states.

- In 4U 1626–67, although the model equations include the systematic uncertainties, and the source distance has a large error, we constrained the mass and radius of the neutron star.

- If the source distance of 4U 1626–67 is determined by some method, we can obtain the information on $R$, and constrain the proposed equation of states.

- If the accretion torque model is improved, we also obtained an accurate value of the mass and radius of the neutron star in 4U 1626–67.

- In X Persei, we found that the surface magnetic field of the neutron star prefer a range of the $B = (4 - 20) \times 10^{13}$ G, by using the accretion torque model proposed by Ghosh & Lamb (1979).

- The obtained result is consistent with a suggestion that the neutron star in X Persei has relatively strong magnetic field of $\sim 10^{13}$ G (Sasano, 2015).

# Appendix A

# ERROR ESTIMATIONS OF PERIODS AND ITS DERIVATIVES

In order to derive a periodicity, e.g., a pulse period and its derivative in binary X-ray pulsars, in light curve data, the epoch folding method presented in § 5.1 is usually employed. Although we can easily derive a period from data, to estimate its error is difficult. Then, we tried to estimate the errors, on which pulse period and its derivatives obtained by the epoch folding method, with various method, and evaluated these values.

## A.1 Method 1 - The Parameter $a$ and the Standard Estimate -

First, we estimate the errors with a straight-forward method, which assumed that the errors $\Delta P$ and $\Delta \dot{P}$ are related to a difference of pulse number $a$ in the total time span $T_{\mathrm{s}}$ of the observation. Then we can express the errors as

$$\Delta P = \frac{aP^2}{T_{\mathrm{s}}}, \ \Delta \dot{P} = \frac{2aP^2}{T_{\mathrm{s}}^{2}}. \tag{A.1}$$

In this case, $a$ is generally less than one pulse. The above equations (equation A.1) can be led by the following explanation. The number of pulses $n(t)$ from $t_0$ to $t$ is calculated by an integral of the pulse frequency $\nu(t)$ from $t_0$ to $t$. In this calculation, we assumed that the frequency $\nu$ only depends on time with a constant $\dot{\nu}$, or we used only the first order of derivatives in Taylor expansion series. By using

61

$v(t') = v_0 + \dot{v}_0(t' - t_0)$, we obtain an equation as

$$n(t) = \int_{t_0}^{t} v(t') \, dt' = v_0(t - t_0) + \frac{\dot{v}_0}{2}(t - t_0)^2. \tag{A.2}$$

Substituting the whole time span $T_s$ for $(t - t_0)$, we derive

$$n(t) = v_0 T_s + \frac{\dot{v}_0}{2} T_s^2. \tag{A.3}$$

The obtained expression (equation A.3) can be considered as a function of $v_0$ and $\dot{v}_0$. Then the "variation of $n(t)$", $\Delta n$, can be described as a function of variations of $\Delta v_0$ and $\Delta \dot{v}_0$,

$$\Delta n(\Delta v_0, \; \Delta \dot{v}_0) = \frac{\partial n(t)}{\partial v_0} \Delta v_0 + \frac{\partial n(t)}{\partial \dot{v}_0} \Delta \dot{v}_0 = T_s \Delta v_0 + \frac{T_s^2}{2} \Delta \dot{v}_0. \tag{A.4}$$

In this section, employing $\Delta n = a$, we derive equations of $\Delta v_0$ and $\Delta \dot{v}_0$,

$$\Delta v_0 = \frac{a}{T_s} \text{ and } \Delta \dot{v}_0 = \frac{2a}{T_s^2}, \tag{A.5}$$

from equation (A.4). Converting $\Delta v_0$ and $\Delta \dot{v}_0$ in equation (A.5) to $\Delta P_0$ and $\Delta \dot{P}_0$, we obtain the equations, which depend on $a$, as

$$\Delta P_0 = \frac{a P_0^2}{T_s} \text{ and } \Delta \dot{P}_0 = \frac{2a P_0^2}{T_s^2} + \frac{2a P_0 \dot{P}_0}{T_s}. \tag{A.6}$$

In our case, we can ignore the second term of $\Delta \dot{P}_0$, the parameters which we used give a condition of $P_0/T_s \gg \dot{P}_0$.

In this appendix, in order to understand the difference among various methods, we employed the value of $a$. In Leahy (1987), $a = 1/2$ called the "standard estimate", and they gave

$$\frac{\Delta P}{P} = \frac{P}{2T_s}. \tag{A.7}$$

Applying the standard estimate ($a = 1/2$) to our case ($T_s = 60$ days $= 5184000$ s, and $P = 7.67$ s), we derived the errors of $P$ and $\dot{P}$ as

$$\Delta P = 5.7 \times 10^{-6} \text{ s and } \Delta \dot{P} = 2.2 \times 10^{-12} \text{ s s}^{-1}. \tag{A.8}$$

However, there is no reason to select $a = 1/2$.

## A.2  Method 2 - A Sinusoidal Pulse Case -

We can easily consider that $a$ should be related to the reduced chi-square ($\chi_v^2$) value, which is calculated from the folded light curve obtained by the epoch folding method. By using the Monte-Carlo simulation, Leahy (1987) derived an empirical relation between $a$ and $\chi_v^2$,

$$\frac{\Delta P}{\Delta P_\mathrm{L}} = 0.71 \left(\chi_v^2 - 1\right)^{-0.63}, \tag{A.9}$$

with assumption of a sinusoidal pulse shape, where $\Delta P_\mathrm{L} = P^2/2T_\mathrm{s}$. In other words, the above equation can be rewritten as

$$a = \frac{1}{2} \times 0.71 \left(\chi_v^2 - 1\right)^{-0.63}. \tag{A.10}$$

When the reduced chi-square is within the range of $\chi_v^2 = 3 - 110$, we can use the equation. In the case of 4U 1626–67, since the obtained reduced chi-square, $\chi_v^2 = 3.48$, is within the range, we can employ equation (A.10), and obtained $a = 0.20$. By using the obtained $a$ and equation (A.6), we calculated the error of $P$ as

$$\Delta P = 2.3 \times 10^{-6} \text{ s}. \tag{A.11}$$

Although the error of $\dot{P}$ was not evaluated in Leahy (1987), we calculated the error from equation (A.10) with an assumption that the calculated $a$ is also effective in this case as

$$\Delta \dot{P} = 0.88 \times 10^{-12} \text{ s s}^{-1}. \tag{A.12}$$

## A.3  Method 2 Modified - Considering the Pulse Shape -

In method 2, since the pulse shape is assumed as a sine function, which has the broadest pulse width with full width at half maximum (FWHM) of 0.5, it is considered to give the worst case among various pulse shapes. In 4U 1626–67, the obtained pulse profile shown in figure A.1 has sharp peaks, FWHM = 0.085, and it can be considered to give a good estimation of periods. If we employ the assumption, the errors of $P$ and $\dot{P}$ would be smaller than that calculated by method 2 by a factor of 0.085/0.5. In this case, we obtained $a = 0.034$ ($a = 0.20 \times 0.085/0.5$), and
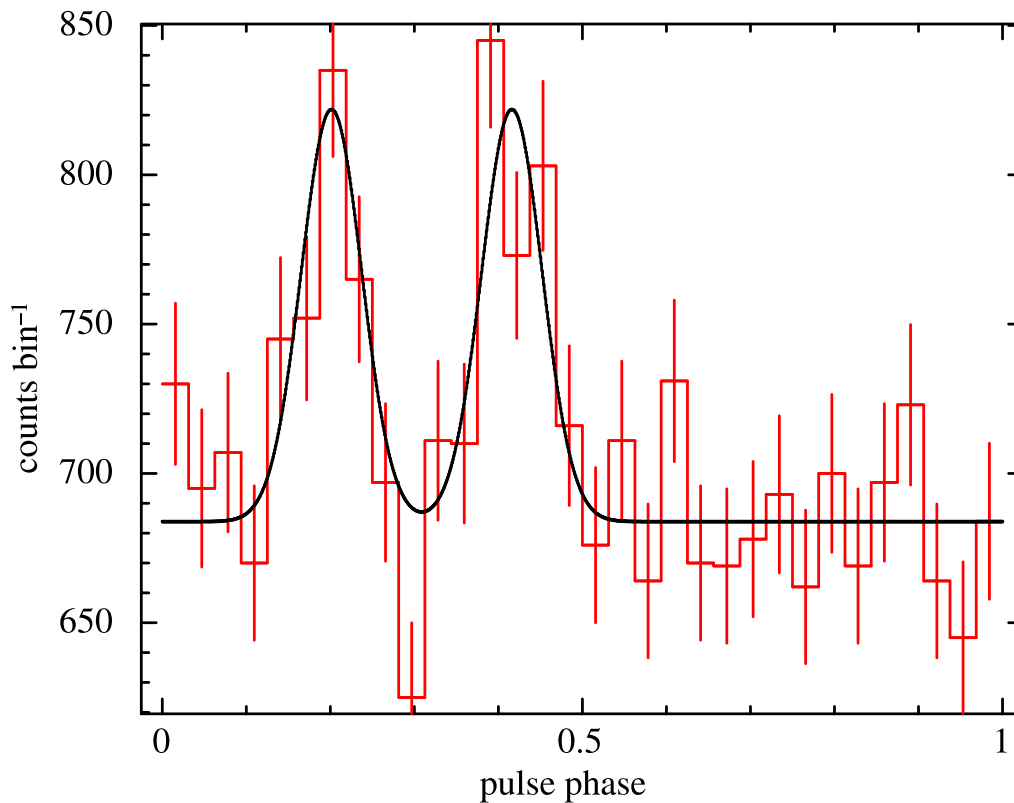
Figure A.1: Observed pulse profile of 4U 1626–67 in 2–10 keV band for MJD 55290–55350, and a pulse profile model, which consists of two gaussian representing the peaks and a constant, with $\chi_\nu^2 = 1.30$ (Takagi et al., 2016). The gaussians have an equal height and width ($\sigma = 0.036$, or FWHM = 0.085). The background rate is 440 counts/bin.

calculated the errors as

$$\Delta P = 0.39 \times 10^{-6} \text{ s and } \Delta \dot{P} = 0.15 \times 10^{-12} \text{ s s}^{-1}, \qquad (A.13)$$

where we ignored the effect that the pulse profile has two peaks.

## A.4    Method 3 - Deviation from the Best Pulse Profile -

When data is fitted with a model with $\chi_\nu^2 \sim 1.0$, we can derive the errors of the parameters in the model. If the method can be applied to the estimation of the errors of $P$ and $\dot{P}$, we obtained the values. Before the method is applied to our case, we should note the following problem. While the parameters in a model are changed to

estimate their errors in the $\chi^2$ fitting method, we calculate distribution of $\chi^2$ varying the trial $P$ and $\dot{P}$, which are employed to make the folded light curve, and estimate the errors from the distribution. First, we searched the best-fit model for the pulse profile, and defined that, which has an acceptable $\chi_\nu^2$, as the model, shown in figure A.1. After that, we calculated the distribution of $\chi^2$, and searched the region within $\chi^2$ of the minimum value plus 1.0, which represents the one-parameter error region for $P$ and $\dot{P}$. Figure A.2 shows the obtained distribution of $\chi^2$. By using the region, we calculated the errors as

$$\Delta P = 0.2 \times 10^{-6} \text{ s and } \Delta\dot{P} = 0.4 \times 10^{-12} \text{ s s}^{-1}. \tag{A.14}$$

We calculated the values of $a$ from the estimated errors of $P$ and $\dot{P}$, and obtained that $a$ is 0.02 and 0.09, respectively.
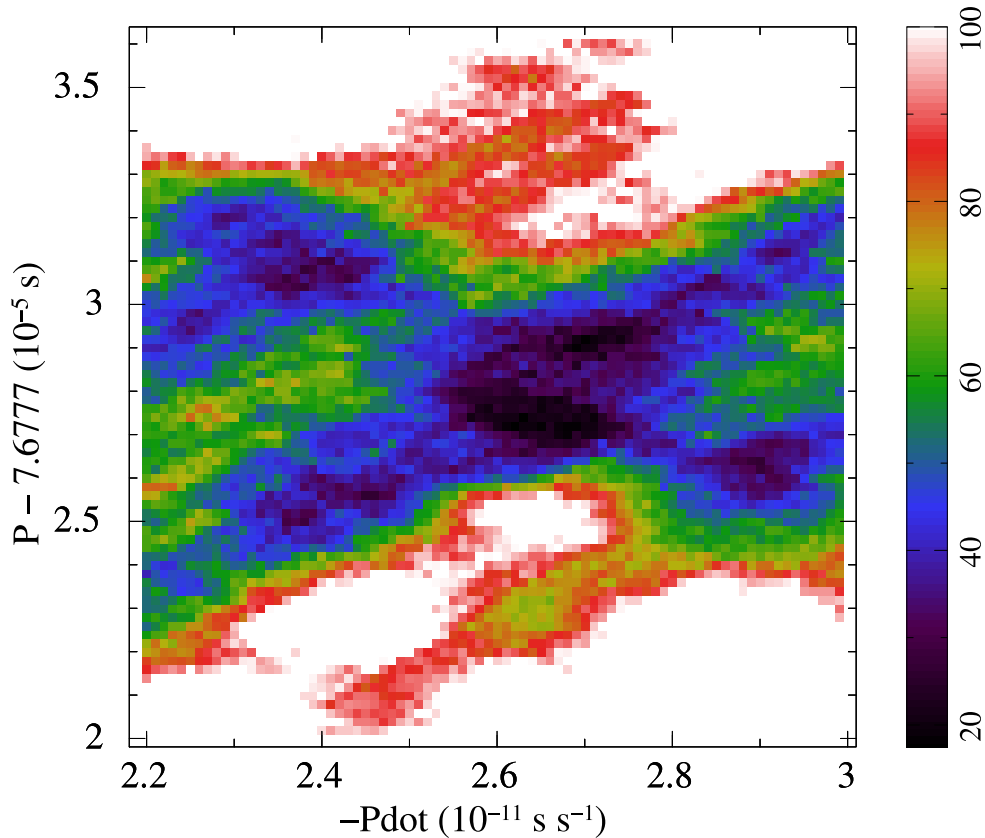


Figure A.2: Distribution of $\chi^2$, which indicates deviation for the assumed pulse model shown in figure A.1 (Takagi et al., 2016). The right bar indicates the $\chi^2$ values. The obtained minimum $\chi^2$ is 17.48.

## A.5 Method 4 - Monte-Carlo Simulation -

We performed Monte-Carlo simulations to make simulated data of X-ray photons, in which all the observational conditions, e.g., source intensity, background intensity, accumulated area, exposure, and transit times of the scans, are considered. We searched the most-likely $P$ and $\dot{P}$ from the simulated data with the epoch folding method, which is the same analysis in the real observation. As an example, the distribution of $\chi^2$ obtained from the simulated data is shown in figure A.3. It has similar distribution and extension in the real case (figure 5.4). Repeating the analysis 200 times, we make a histogram of $P$ and $\dot{P}$ obtained from each simulated data, shown in figure A.4. In order to estimate the errors of $P$ and $\dot{P}$, we fitted the histogram with the gaussian model, and calculated the 1-$\sigma$ errors as

$$\Delta P = 0.48 \times 10^{-6} \text{ s and } \Delta\dot{P} = 0.63 \times 10^{-12} \text{ s s}^{-1}. \tag{A.15}$$

We calculated the values of $a$ from the estimated errors of $P$ and $\dot{P}$, and obtained that $a$ is 0.042 and 0.14, respectively. We performed this simulation for each 60-d interval, which corresponds to the intervals of the real case.

## A.6 Discussion

By using the several method, we calculated the errors of $P$ and $\dot{P}$ ($\Delta P$, $\Delta\dot{P}$) obtained by the epoch folding method. In this appendix, we showed the test case of the MAXI observation of 4U 1626–67 from MJD 55290 to MJD 55350. The obtained results are summarized in table A.1 and figure A.5. If the pulse profile is sinusoidal, the error of $P$ calculated by Method 2 would be only appropriate. Since the peak width of the observed pulse profile is sharper than that of a sinusoidal pulse, the error in that case is considered to be a "loose error" or conservative error. Considering the width of the pulse profile, we obtained the error, which is similar to that by the Monte-Carlo simulation, although it is not exactly the same. In the case of the error of $\dot{P}$, the error calculated by Method 2 is the closest one. If we employed the Monte-Carlo simulation, $a$ for the error of $\dot{P}$, which is 3 times larger $a$ for that of $P$, is derived, although the reason why the result was obtained is unclear. Evaluating the errors of $P$ and $\dot{P}$ estimated by various methods, we finally employed these obtained by the Monte-Carlo simulation. We also performed the same analysis for another span (MJD 56250–56310), and listed the obtained results in table **??**. We found almost the same relation in that span.
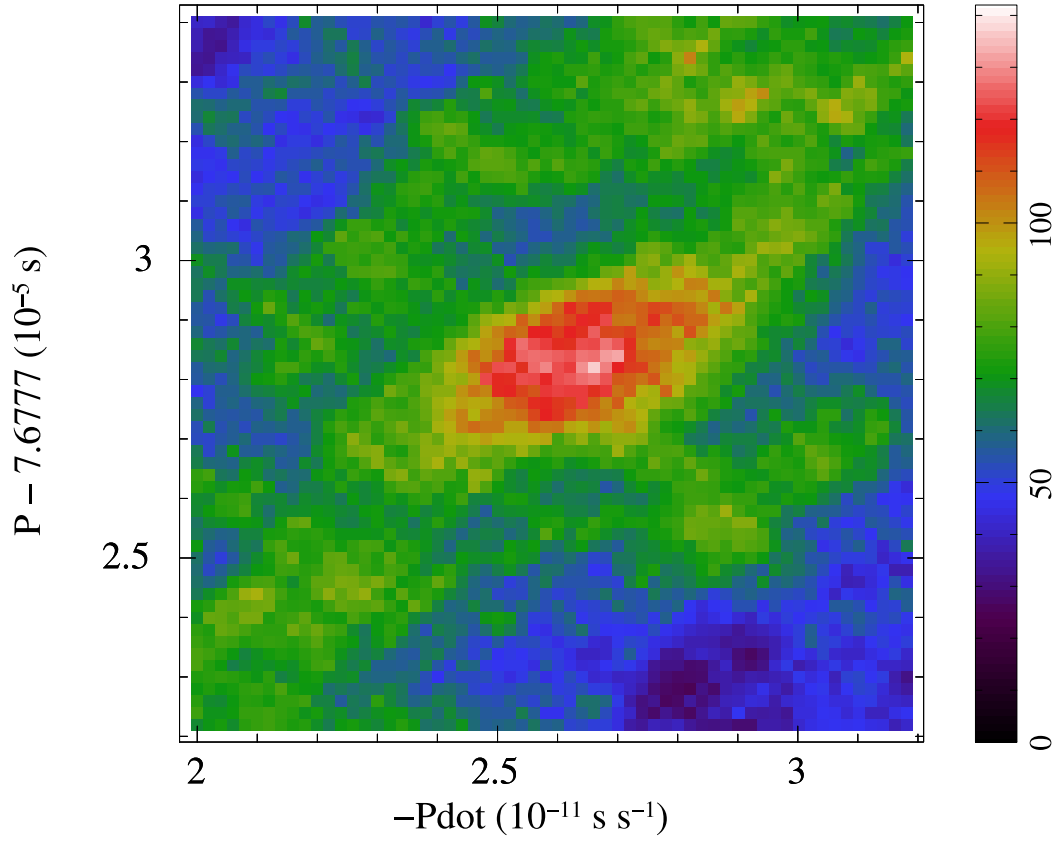
Figure A.3: Distribution of $\chi^2$ calculated from the simulated data with the same observation condition for MJD 55290–55350 (Takagi et al., 2016). The right bar indicates the $\chi^2$ values. The maximum $\chi^2$ is 137 for 31 degrees of freedom at $P = 7.6777282$ s and $\dot{P} = -2.66 \times 10^{-11}$ s s$^{-1}$.
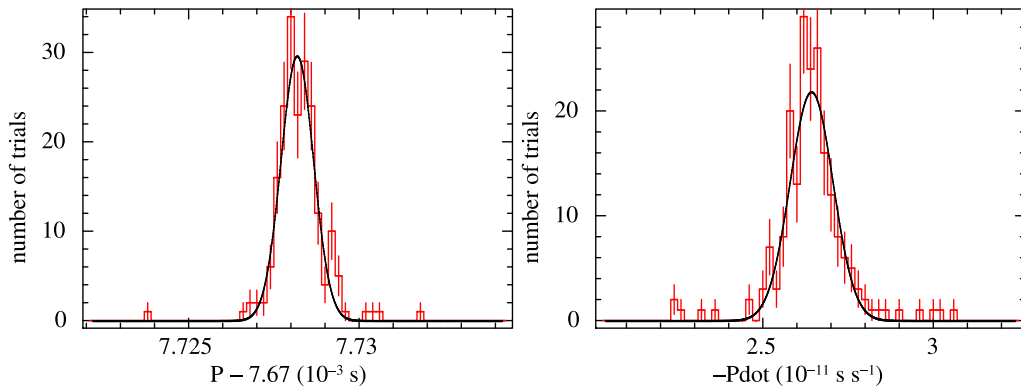


Figure A.4: Histograms of $P$ (left) and $\dot{P}$ (right) obtained from the simulated data (Takagi et al., 2016). The number of trials is 200.

Table A.1: Errors of $P$ and $\dot{P}$ in MJD 55290–55350.

| Method | $\Delta P$ $(10^{-6}$ s) | $\Delta \dot{P}$ $(10^{-12}$ s s$^{-1})$ | $a$ |
|---|---|---|---|
| 1 "standard" | 5.7 | 2.2 | 0.5 |
| 2 Leahy | 2.3 | (0.88)[1] | 0.20 |
| 2 modified | 0.39 | (0.15)[1] | 0.034 |
| 3 pulse fit | 0.2 | 0.4 | 0.02[2], 0.09[3] |
| 4 MC | 0.48 | 0.63 | 0.042[2], 0.14[3] |

[1] $\Delta \dot{P}$ is not given in Leahy (1987).
[2] Calculated from $P$.
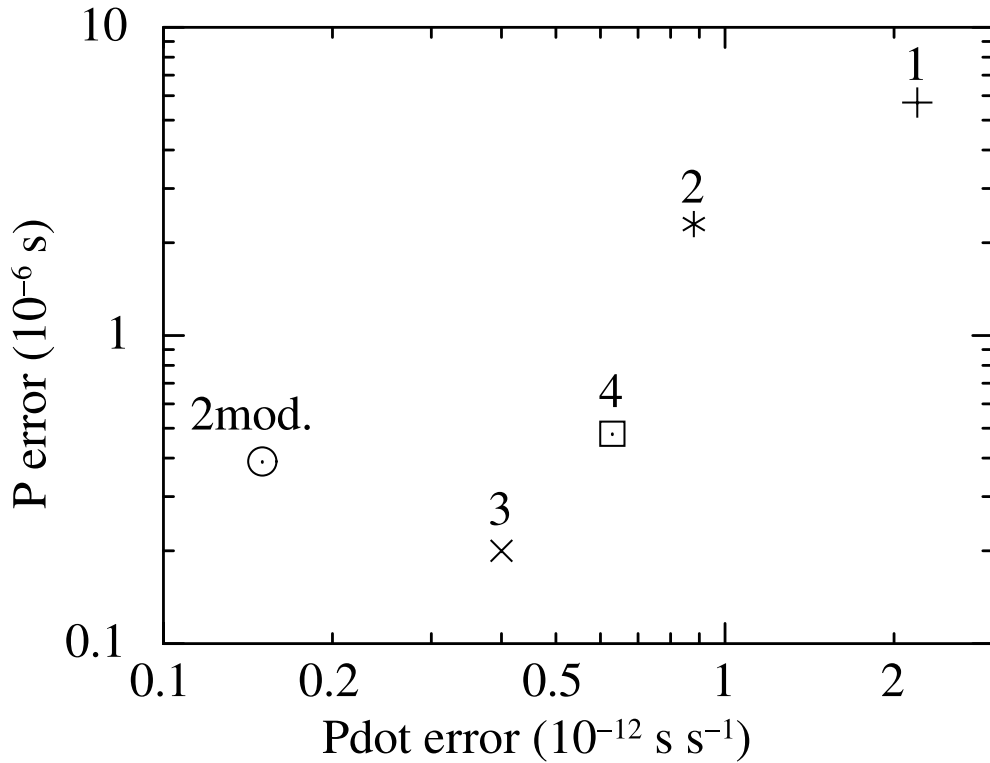[3] Calculated from $\dot{P}$.



Figure A.5: Errors of $P$ and $\dot{P}$ obtained by various methods (Takagi et al., 2016). The numbers in the figure express the methods.

Table A.2: Errors of $P$ and $\dot{P}$ in MJD 56250–56310.

| Method | $\Delta P$ | $\Delta \dot{P}$ | $a$ |
|---|---|---|---|
| | $(10^{-6}$ s$)$ | $(10^{-12}$ s s$^{-1})$ | |
| 1 "standard" | 5.7 | 2.2 | 0.5 |
| 2 Leahy | 3.3 | $(1.3)^1$ | 0.29 |
| 2 modified | 0.56 | $(0.21)^1$ | 0.049 |
| 3 pulse fit[2] | – | – | –, – |
| 4 MC | 0.90 | 1.07 | $0.079^3$, $0.24^4$ |

[1] $\Delta \dot{P}$ is not given in Leahy (1987).
[2] $\chi^2$ minimum region could not be determined.
[3] Calculated from $P$.
[4] Calculated from $\dot{P}$.

# ACKNOWLEDGEMENT

# Bibliography

Acuner, Z., İnam, S. Ç., Şahiner, Ş., et al. 2014, MNRAS, 444, 457

Akmal, A., Pandharipande, V. R., & Ravenhall, D. G. 1998, Phys. Rev. C, 58, 1804

Angelini, L., White, N. E., Nagase, F., et al. 1995, ApJ, 449, L41

Baade, W., & Zwicky, F. 1934, Proceedings of the National Academy of Science, 20, 254

Basko, M. M., & Sunyaev, R. A. 1975, A&A, 42, 311

Baym, G., & Pethick, C. 1979, Annual Review of Astronomy and Astrophysics, 17, 415

Bhattacharyya, S. 2010, Advances in Space Research, 45, 949

Bildsten, L., Chakrabarty, D., Chiu, J., et al. 1997, ApJS, 113, 367

Bozzo, E., Stella, L., Vietri, M., & Ghosh, P. 2009, A&A, 493, 809

Camero-Arranz, A., Finger, M. H., Ikhsanov, N. R., Wilson-Hodge, C. A., & Beklen, E. 2010, ApJ, 708, 1500

Camero-Arranz, A., Pottschmidt, K., Finger, M. H., et al. 2012, A&A, 546, AA40

Chakrabarty, D. 1998, ApJ, 492, 342

Chakrabarty, D., Bildsten, L., Grunsfeld, J. M., et al. 1997, ApJ, 474, 414

Delgado-Martí, H., Levine, A. M., Pfahl, E., & Rappaport, S. A. 2001, ApJ, 546, 455

Demorest, P. B., Pennucci, T., Ransom, S. M., Roberts, M. S. E., & Hessels, J. W. T. 2010, Nature, 467, 1081

Di Salvo, T., Burderi, L., Robba, N. R., & Guainazzi, M. 1998, ApJ, 509, 897

Doroshenko, V., Santangelo, A., Kreykenbohm, I., & Doroshenko, R. 2012, A&A, 540, L1

Douchin, F., & Haensel, P. 2001, A&A, 380, 151

Elsner, R. F., Darbro, W., Leahy, D., et al. 1983, ApJ, 266, 769

Finger, M. H., Wilson, R. B., & Chakrabarty, D. 1996, A&AS, 120, 209

Ghosh, P., & Lamb, F. K. 1979, ApJ, 234, 296

Giacconi, R., Gursky, H., Kellogg, E., Schreier, E., & Tananbaum, H. 1971, ApJL, 167, L67

Giacconi, R., Gursky, H., Paolini, F. R., & Rossi, B. B. 1962, Physical Review Letters, 9, 439

Giacconi, R., Murray, S., Gursky, H., et al. 1972, ApJ, 178, 281

Hewish, A., Bell, S. J., Pilkington, J. D. H., Scott, P. F., & Collins, R. A. 1968, Nature, 217, 709

Iwakiri, W. B., Terada, Y., Mihara, T., et al. 2012, ApJ, 751, 35

Jain, C., Paul, B., & Dutta, A. 2010, MNRAS, 403, 920

Joss, P. C., & Rappaport, S. A. 1984, ARA&A, 22, 537

Kii, T., Hayakawa, S., Nagase, F., Ikegami, T., & Kawai, N. 1986, PASJ, 38, 751

Kirsch, M. G., Briel, U. G., Burrows, D., et al. 2005, Proc. SPIE, 5898, 22

Klochkov, D., Staubert, R., Postnov, K., Shakura, N., & Santangelo, A. 2009, A&A, 506, 1261

Klus, H., Ho, W. C. G., Coe, M. J., Corbet, R. H. D., & Townsend, L. J. 2014, MNRAS, 437, 3863

Krauss, M. I., Schulz, N. S., Chakrabarty, D., Juett, A. M., & Cottam, J. 2007, ApJ, 660, 605

Lattimer, J. M., & Schutz, B. F. 2005, ApJ, 629, 979

Leahy, D. A. 1987, A&A, 180, 275

Levine, A., Ma, C. P., McClintock, J., et al. 1988, ApJ, 327, 732

Lovelace, R. V. E., Romanova, M. M., & Bisnovatyi-Kogan, G. S. 1995, MNRAS, 275, 244

Lutovinov, A., Tsygankov, S., & Chernyakova, M. 2012, MNRAS, 423, 1978

Makishima, K., Mihara, T., Nagase, F., & Tanaka, Y. 1999, ApJ, 525, 978

Matsuoka, M., Kawasaki, K., Ueno, S., et al. 2009, PASJ, 61, 999

Mavromatakis, F. 1994, A&A, 285, 503

Mihara, T. 1995, Ph.D. Thesis, Dept. of Physics, Univ. of Tokyo

Mihara, T., Nakajima, M., Sugizaki, M., et al. 2011, PASJ, 63, 623

Oppenheimer, J. R., & Volkoff, G. M. 1939, Physical Review, 55, 374

Orlandini, M., Dal Fiume, D., Frontera, F., et al. 1998, ApJ, 500, L163

Özel, F. 2013, Reports on Progress in Physics, 76, 016901

Özel, F., & Freire, P. 2016, Annual Review of Astronomy and Astrophysics, 54, 401

Pandharipande, V. R., Pines, D., & Smith, R. A. 1976, ApJ, 208, 550

Pines, D. 1980, Science, 207, 597

Pravdo, S. H., White, N. E., Boldt, E. A., et al. 1979, ApJ, 231, 912

Rappaport, S., & Joss, P. C. 1977, Nature, 266, 683

Rappaport, S., Markert, T., Li, F. K., et al. 1977, ApJ, 217, L29

Reynolds, A. P., Parmar, A. N., Stollberg, M. T., et al. 1996, A&A, 312, 872

Sanano, M. 2015, Ph.D. Thesis, Dept. of Physics, Univ. of Tokyo

Shakura, N. I., & Sunyaev, R. A. 1973, A&A, 24, 337

Shen, H., Toki, H., Oyamatsu, K., & Sumiyoshi, K. 1998a, Nuclear Physics A, 637, 435

Shen, H., Toki, H., Oyamatsu, K., & Sumiyoshi, K. 1998b, Progress of Theoretical Physics, 100, 1013

Shinoda, K., Kii, T., Mitsuda, K., et al. 1990, PASJ, 42, L27

Sugizaki, M., Mihara, T., Serino, M., et al. 2011, PASJ, 63, 635

Sugizaki, M., Yamamoto, T., Mihara, T., Nakajima, M., & Makishima, K. 2015, PASJ, 67, 73

Takagi, T., Mihara, T., Sugizaki, M., Makishima, K., & Morii, M. 2016, PASJ, 68, S13

Tomida, H., Tsunemi, H., Kimura, M., et al. 2011, PASJ, 63, 397

van Haaften, L. M., Voss, R., & Nelemans, G. 2012, A&A, 543, A121

Vaughan, B. A., & Kitamoto, S. 1997, arXiv:astro-ph/9707105

Wasserman, I., & Shapiro, S. L. 1983, ApJ, 265, 1036

White, N. E., Mason, K. O., Sanford, P. W., & Murdin, P. 1976, MNRAS, 176, 201

Yagi, K., & Yunes, N. 2013, Phys. Rev. D, 88, 023009